POLITECNICO DI TORINO
Repository ISTITUZIONALE

Numerical characterization of ammonia–hydrogen combustion in internal combustion engines using ECFM under RANS and LES frameworks

Original
Numerical characterization of ammonia–hydrogen combustion in internal combustion engines using ECFM under RANS and LES frameworks / Sola, R., Misul, D., Baratta, M., Mounaïm-Rousselle, C., Brequigny, P., Colin, O.. - In: FUEL. - ISSN 0016-2361. - (2026). [10.1016/j.fuel.2026.141990]

Availability:
This version is available at: 11583/3017624 since: 2026-11-06T12:59:34Z

Publisher:
Elsevier

Published
DOI:10.1016/j.fuel.2026.141990

Terms of use:

This article is made available under terms and conditions as specified in the corresponding bibliographic description in the repository

Publisher copyright

(Article begins on next page)

21 November 2026

Fuel 431 (2027) 141990



Contents lists available at ScienceDirect

Fuel

journal homepage: www.elsevier.com/locate/jfue



Full Length Article

Numerical characterization of ammonia–hydrogen combustion in internal combustion engines using ECFM under RANS and LES frameworks

Riccardo Sola [a,*], Daniela Misul [a], Mirko Baratta [a], Christine Mounaïm-Rousselle [b], Pierre Brequigny [b], Olivier Colin [c]

[a] Politecnico di Torino, Corso Duce degli Abruzzi 24, Torino, 10129, Italy
[b] Univ. Orléans, INSA-CVL, EA 4229 - PRISME, Orléans, F-45072, France
[c] Institut Carnot IFPEN Transports Energie, IFPEN, 1-4 av. du Bois Preau, Rueil-Malmaison, 92852, France

HIGHLIGHTS

- A comprehensive study of a fully premixed combustion internal combustion engine with the well-established combustion model ECFM.
- Combustion of different ammonia/hydrogen mixtures with varying hydrogen content and equivalence ratio.
- Flamelet-based modelling with two different turbulence modelling approaches (RANS and LES).
- Validation of the flamelet-based model under high Karlovitz number combustion regimes.

ARTICLE INFO

Keywords:
CFD
High Karlovitz
Ammonia and hydrogen combustion
Premixed combustion modelling

ABSTRACT

The transition towards low-carbon transport has accelerated the exploration of carbon-free alternative fuels for internal combustion engine applications. Among these, ammonia enriched with hydrogen represents a promising candidate for application in internal combustion engines. In this context, computational fluid dynamics (CFD) plays a pivotal role in supporting engine design; consequently, the predictive capability of the combustion model is of primary importance, particularly within a fuel-flexible framework.

In the present work, a numerical campaign is conducted and validated against an extensive experimental dataset obtained from a commercial light-duty engine operated in a single-cylinder configuration and fuelled with NH_3/H_2 mixtures. The dataset spans a wide range of equivalence ratios and intake pressures. The adoption of a fully premixed charge, together with precise control of engine speed, enables the decoupling of turbulence effects from those associated with mixture properties, thereby allowing a more rigorous assessment of the combustion process. The well-established ECFM combustion model is systematically investigated using both Reynolds-Averaged Navier–Stokes (RANS) and Large Eddy Simulation (LES) turbulence modelling approaches, while maintaining a consistent formulation. Results indicate that model calibration is required to accurately reproduce experimental observations when varying hydrogen content and equivalence ratio. Notably, similar calibration trends are observed for both RANS and LES simulations, suggesting that the required adjustments are primarily linked to the turbulence–flame interaction, as modelled through the flame surface density (Σ) transport equation, rather than to the specific turbulence closure.

These findings highlight the need for an improved formulation of the flame surface density model, capable of adapting to variations in mixture composition and accurately capturing both strain- and curvature-induced flame stretch. Furthermore, the incorporation of a dedicated sub-model to account for flame instabilities, particularly under lean conditions, is shown to be essential for enhancing predictive accuracy.

* Corresponding author.
Email address: riccardo.sola@polito.it (R. Sola).

https://doi.org/10.1016/j.fuel.2026.141990
Received 1 July 2026; Received in revised form 29 September 2026; Accepted 29 October 2026
0016-2361/© 2026 Published by Elsevier Ltd.

Nomenclature

$AHRR$	Apparent heat release rate
AMR	Adaptive mesh refinement
$ATDC$	After top dead centre
BC	Boundary conditions
CAD	Crank angle degree
COV($IMEP$)	Coefficient of variation of IMEP
C_{k+}	Efficiency function
Da	Damköhler number
DNS	Direct numerical simulation
$ECFM$	Extended coherent flame model
IC	Initial conditions
$IMEP$	Indicated Mean Effective Pressure
$ISSIM$	Imposed stretch spark ignition model
Ka	Karlovitz number
LES	Large eddy simulation
LFS	Laminar flame speed
LSR	Length Scale Resolution
MFB	Mass fraction burnt
N_i	Normal to the isosurface of the filtered progress variable (LES)
$RANS$	Reynolds-Averaged Navier-Stokes
$RMSE$	Root mean square error
S_d	Displacement speed (LES)
S_l^0	Unstretched laminar flame speed
S_t	Turbulent flame speed
TCI	Turbulence-Chemistry interaction
l_t	Turbulent length scale
k	Turbulent kinetic energy
u'	Turbulent velocity fluctuation
x_{H_2}	Hydrogen volume fraction in the fuel mixture
α	Alpha stretch parameter
$\tilde{c}$	Volume progress variable
$\tilde{c}_\Sigma$	Progress variable due to flame propagation
ϵ	Turbulent dissipation rate
$\tilde{\kappa}$	Flame front curvature
ϕ	Equivalence ratio
ρ_b	Burnt density
ρ_u	Unburnt density
Σ	Flame surface density
$\tilde{u}_i$	Favre-averaged velocity component

1. Introduction

In the pursuit of substantial greenhouse gas emission reductions within the transport sector and the transition towards a carbon-neutral energy system, internal combustion engines (ICEs) operating on alternative fuels emerge as a practical and scalable medium-term solution. Among the potential candidates, ammonia has gained increasing attention as a carbon-free energy carrier, owing to its favourable storage and handling characteristics relative to hydrogen, as well as its capability to serve as an efficient hydrogen vector. Recent advancements in combustion research have demonstrated the technical feasibility of utilizing ammonia and ammonia–hydrogen blends in ICEs, highlighting their potential to enable cleaner and more sustainable propulsion systems. Despite its potential, the inherently low reactivity of neat ammonia–air mixtures poses a significant challenge for direct application in spark-ignition engines, particularly under lean operating conditions. This limitation is commonly addressed through the addition of hydrogen, which effectively enhances mixture reactivity, promotes higher laminar flame speeds, and improves combustion stability, especially at low engine loads. Consequently, ammonia–hydrogen blends have emerged as a more viable fuel option for practical engine operation. In this context, recent review studies have extensively examined the fundamental chemical kinetics of ammonia combustion alongside its implementation in internal combustion engines, offering comprehensive evaluations of performance characteristics and emission behaviour [1]. Several studies have explored the fundamental chemical and combustion characteristics of ammonia and ammonia–hydrogen blends [2], revealing marked differences compared to conventional hydrocarbon fuels. These distinct properties necessitate the development of tailored combustion strategies, as well as adaptations in engine design and modelling approaches. To further elucidate the performance and operability of ammonia-based fuels, numerous experimental campaigns have been conducted, focusing on engine efficiency and combustion stability across a wide range of operating conditions and mixture compositions. A key objective of these studies has been to minimize the hydrogen fraction in the fuel blend, thereby simplifying onboard storage requirements and reducing overall hydrogen demand [3,4]. In addition, hydrogen enrichment has been shown to play a critical role in influencing combustion stability, pollutant formation pathways, and unburned ammonia emissions [5]. Notably, an extensive experimental campaign conducted at the University of Orléans explored various engine configurations and fuel compositions, including partially cracked ammonia blends, where hydrogen was added to ammonia upstream of the engine to replicate the composition obtained from ammonia cracking [6–8]. These studies provide valuable insights into the practical implementation and optimization of ammonia-based fuel systems.

A more detailed experimental investigation was conducted in a spherical vessel to analyse the initial development of the flame kernel under laminar conditions, focusing on the stretch sensitivity of different NH3/H2 mixtures [9,10]. In particular, non-monotonic trends were observed when varying the hydrogen content in lean ammonia-based mixtures, highlighting how flame stretch behaviour strongly depends on mixture composition. In addition, turbulence–flame interaction was investigated by introducing isotropic turbulence within the vessel [11]. In the latter work, a new correlation linking the Karlovitz number to variations in turbulent flame speed was identified, demonstrating how non-dimensional parameters describing both mixture chemistry and turbulence properties can effectively characterize turbulent flame propagation behaviour. Similar findings were previously reported by Lapointe et al. [12], who investigated different fuels and equivalence ratios through two-dimensional direct numerical simulations. Their study focused on heavier fuels, with differential diffusion effects systematically isolated by tuning the Lewis number. By taking advantage of the DNS framework, these studies enable a detailed analysis of flame geometry, allowing the stretch contributions to be separated into curvature (both positive and negative) and strain rate effects across the flame front. These aspects are of fundamental importance from a modelling perspective, particularly in the context of the combustion model investigated in this work. In fact, understanding how fuel composition and mixture conditions influence flame geometry and stretch is essential for accurately predicting turbulence–flame interaction under varying turbulence and mixture conditions. Similar DNS studies on ammonia–hydrogen blends have recently been reported. Highly resolved two-dimensional DNS simulations were performed to investigate the onset and evolution of flame instabilities in ammonia–hydrogen mixtures under different operating conditions [13,14]. Despite ammonia generally tending to stabilize flame behaviour, instabilities are observed in sufficiently lean mixtures, confirming a non-monotonic response with respect to variations in the fuel blend ratio in NH_3/H_2/air flames. On the other

hand, three-dimensional DNS simulations provide more representative conditions to accurately assess turbulence–flame interaction, as well as flame instabilities and their coupling with flame stretch sensitivity [15,16]. These studies offer a detailed characterization of flame geometry under varying mixture compositions and properties. In particular, they clearly demonstrate that a premixed combustion model aiming to accurately predict flame propagation under varying mixture and turbulence conditions must account for the coupled interaction between flame stretch evolution, including both strain-induced and curvature-induced contributions, and flame instabilities, especially under lean conditions. In addition, a new modelling approach for the stretch factor has been proposed by [16], based on one-dimensional counterflow flame simulations. This formulation does not rely on ad hoc correlations, making the model theoretically applicable across a wide range of fuel mixtures. In this context, the present work aims, on the one hand, to assess whether the selected combustion model is capable of accurately reproducing the combustion process in terms of flame propagation and total flame stretch. On the other hand, the predictive capability of the model is evaluated by analysing the extent to which calibration is required when varying mixture composition and operating conditions. This work represents the continuation of previous studies conducted by the PT-ERC group at Politecnico di Torino, primarily focused on the transition between combustion regimes through passive pre-chamber combustion systems fuelled by hydrogen and methane blends under both stoichiometric and lean operating conditions [17]. Recently, a comparison between the ECFM and G-equation models was presented using the same engine configuration investigated in this work, fuelled by ammonia/hydrogen blends. The study evaluated the predictive capability of these two flamelet-based combustion models when varying hydrogen content and equivalence ratio [18]. The present work represents a further development of this investigation, providing a deeper analysis of combustion regime transitions with the aim of moving towards a fully predictive combustion modelling approach.

After describing the experimental apparatus and engine setup, the ECFM combustion model adopted in this study is presented in detail, together with the numerical setup and methodology, in Section 3. This model is particularly appropriate for premixed combustion, as it describes turbulence–flame interaction through the modelling of flame stretch, distinguishing between strain-induced and curvature-induced contributions [19]. In Section 4, the numerical results are extensively discussed for all investigated mixtures and operating conditions. The analysis first considers the RANS turbulence approach, followed by LES simulations for selected operating points, in order to assess the sensitivity of the combustion model to the turbulence description. The same combustion model formulation is retained for both RANS and LES approaches, with only minor adaptations to account for differences in the resolved turbulent field [20]. A detailed analysis of each source term in the combustion model transport equations is also performed by comparing RANS and LES results for a representative operating condition. In addition, a comprehensive mesh sensitivity analysis is carried out to evaluate the influence of mesh resolution throughout the full engine cycle and its effect on the predicted combustion process. For the LES approach, the influence of AMR on the estimation of u' during the combustion process is analysed in detail to assess the sensitivity of the combustion model to the evolution of the resolved turbulent field.

2. Engine setup

The engine specifications are described in detail by Lhuillier et al. [6,7] and summarized in Table 1. Briefly, the experiments were conducted on a single-cylinder 4-valve light duty engine fuelled with an air–fuel mixture, as schematized in Fig. 1. The main shaft is equipped with a Kübler optical encoder, providing angular position measurements with a resolution of 0.1 crank angle degrees (CAD). In-cylinder pressure is measured using a water-cooled AVL piezoelectric transducer, with the same angular resolution and a measurement range of 0–25 MPa. Intake

Table 1
Engine specifications and test-bench setup.

Engine specifications	
Model	PSA EP6DT
Stroke	85.8 mm
Bore	77 mm
Connecting road length	138.5 mm
Displacement volume	399.5 cm^3
geometric compression ratio	10.5:1
Valves	4
Engine speed	1500 rpm

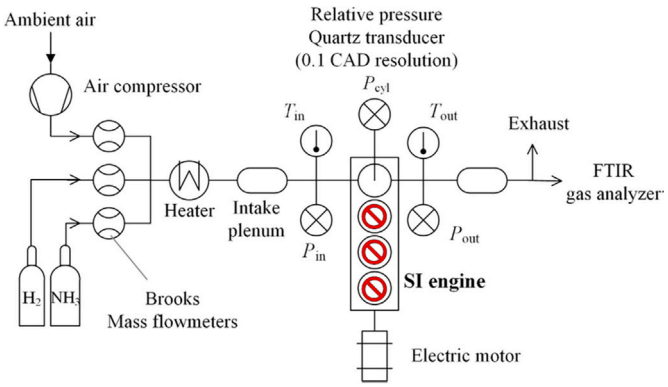


Fig. 1. Experimental apparatus.

and exhaust pressures and temperatures are monitored using type K thermocouples and piezo-resistive pressure sensors. Absolute cylinder pressure is determined by referencing the in-cylinder pressure to the mean intake pressure (Pin) at 20 CAD during the intake stroke. The original spark plug is used, with a coil charging time set to 2 ms. The mixture was prepared upstream of the intake plenum to ensure fully premixed conditions. An electric heater was used to control the intake temperature (fixed to 323 K), thereby maintaining consistent mixture conditions across all experimental runs. The engine was driven by an electric motor at a fixed speed of 1500 rpm. For each operating condition, 100 consecutive engine cycles were acquired. Data acquisition was initiated only after the exhaust gas temperature had reached steady-state conditions.

The hydrogen and ammonia flow rates were measured using Brooks thermal mass flow meters with an accuracy of ±0.7%, together with the air mass flow rate, to ensure precise control of the mixture in terms of equivalence ratio and hydrogen concentration in the fuel. In addition, the air flow controller was used to gradually vary the intake pressure, enabling precise control of the engine load. The combination of a fixed engine speed and fully controllable intake pressure also allowed stable turbulence within the engine, which is particularly important for the subsequent numerical analysis. The spark timing was set to achieve the highest net indicated mean effective pressure (IMEP). All acquired points satisfied the stability criterion, maintaining a Coefficient of Variation of IMEP [COV(IMEP)] below 5%. The experimental operating conditions are summarized in Table 2. Not all combinations listed in Table 2 were experimentally reachable due to stability limits, as the COV(IMEP) approached the threshold. In particular, mixtures with lower hydrogen concentrations could not operate under the leanest conditions. Moreover, only a few operating points were tested at 0.6 and 0.8 bar intake pressure to evaluate the model performance under intake pressure variations, which lead to different turbulence intensity levels while maintaining the same fuel mixture. Throughout the paper, all feasible combinations are presented and compared with numerical results, particularly those near the stability limit. These engine specifications were kept constant throughout the numerical analysis presented in the following sections.

Table 2
Experimentally investigated engine operating conditions.

Operating conditions	
Intake temperatures	323 K
Intake pressures	[0.6–1.2] bar
Equivalence ratios	[0.6–1.2]
H2 M fraction in the fuel x_{H_2}	[0–0.6]
SI timing	MBT

3. Numerical methodology

3.1. Numerical setup

All numerical simulations presented in this study were performed using the CONVERGE 4.1.2 CFD code, employing a density-based PISO algorithm to solve the conservation equations for compressible flow. In accordance with the flamelet modelling approach, single-species diffusion properties were adopted, as no fuel injection or in-cylinder mixing occurs during the simulations. The temporal discretisation was controlled by imposing a velocity-based CFL number of 1. Accordingly, the time step was dynamically adjusted based on the local velocity field throughout the simulation. Consistent with the experimental setup, a fully premixed mixture enters the computational domain through the intake port. The mixing process takes place upstream of the engine, within the intake piping and plenum, as described previously. This subsection summarizes the numerical models adopted in all simulations. The same combustion model, described in detail in a subsequent section, was applied together with two different turbulence modelling approaches. Specifically, both Reynolds-Averaged Navier–Stokes (RANS) and Large Eddy Simulation (LES) frameworks were used to assess the influence of turbulence on the combustion model performance. Accordingly, the numerical settings were adapted to be consistent with each turbulence approach. Further details are provided in the following sections. Table 3 summarizes the numerical models employed in the simulations. For the RANS calculations, the renormalization group (RNG) $k-\varepsilon$ turbulence model [21] was adopted, whereas the Smagorinsky model was used within the LES framework [22]. The GruMO-UniMORE heat transfer model [23] was used to estimate wall heat losses throughout the engine cycle.

Mesh generation was performed automatically at each time step, starting from a base grid size of 4.0 mm and refined using both available refinement strategies. Local fixed embeddings were applied to selectively refine specific regions and volumes associated with key engine events, such as valve opening and closing and the combustion process. Consistently, several of these refinements were activated cyclically during successive engine cycles. In addition, adaptive mesh refinement (AMR) was employed to dynamically refine regions characterized by high velocity gradients and to accurately resolve the flame front during combustion.

Table 4 summarizes the mesh strategy adopted in this study, reporting the minimum cell sizes applied in all numerical simulations presented in this work. The table also highlights the differences between the LES and RANS mesh configurations. The mesh strategy was defined following best practices established in the literature for the simulation of premixed combustion in spark-ignition engines using both RANS and LES approaches. For the RANS framework, a dedicated mesh sensitivity analysis was conducted to evaluate the influence of the mesh resolution over the entire engine cycle using three different base mesh sizes. In addition to the reference mesh (4.0 mm), two additional configurations were considered: a finer mesh (2.0 mm) and a coarser mesh (6.0 mm). Since all refinement levels depend on the base mesh size, modifying the base mesh resulted in corresponding changes to all derived mesh refinements. Fig. 3 and Table 5 show the in-cylinder pressure profiles over two consecutive cycles and the corresponding engine parameter variations for different mesh resolutions, both over the full engine cycle and zoomed in on the combustion phase. The results indicate that no significant differences are observed among the three mesh configurations. For the LES analysis, a mesh sensitivity study focused on the combustion phase was conducted to assess the influence of the grid strategy on the prediction of flame front propagation. In addition, the Length Scale Resolution (LSR) parameter was monitored to evaluate whether the grid resolution is sufficient to resolve an adequate portion of the turbulence spectrum, in accordance with LES best practices. The LSR parameter compares the filter size (i.e., the grid size) with the Kolmogorov length scale and is defined as $LSR = \frac{\Delta}{60\eta}$, where η represents the Kolmogorov length scale, estimated as $\eta \simeq \frac{L_0}{Re^{3/4}}$, with L_0 being the integral length scale of the flow and Re the Reynolds number [27]. The LSR parameter is proportional to the deviation between the actual resolved energy level and the corresponding lower limit of the inertial subrange. It therefore provides an indication of the consistency between the adopted mesh size and the local resolution of the turbulent kinetic energy throughout the computational domain. Pope also proposed the so-called Pope index, M, defined as $M = \frac{k_{sgs}(x;t)}{k_{sgs}(x;t)+k_{res}(x;t)}$, which compares the subgrid-scale kinetic energy, k_{sgs}, associated with unresolved turbulent eddies, with the total turbulent kinetic energy, given by the sum of the resolved contribution, k_{res}, and the subgrid-scale contribution [27]. The evaluation of this index requires a statistically converged solution over the engine cycle, which in turn requires a sufficiently large number of simulated cycles to accurately determine the resolved velocity fluctuations from the resolved velocity field. Since five consecutive cycles are not sufficient for a statistically robust evaluation of the Pope index, mesh quality is assessed here solely through the LSR parameter, which provides a suitable alternative [28]. The LSR parameter is typically expected to remain below 3/5. In the present simulations, the LSR parameter remains below 1, suggesting that the adopted grid resolution is sufficiently fine to resolve the relevant portion of the turbulence spectrum. Fig. 2 shows a snapshot of the LSR field during the intake phase, when the turbulence intensity reaches its highest values. The results show that the LSR parameter remains below 1 throughout the cylinder volume, and is therefore well below the recommended upper limit reported by [28]. This provides further support for the adequacy of the adopted mesh resolution for resolving the relevant turbulent structures during the engine cycle.

Moreover, previous studies have demonstrated that the total flame surface predicted by the ECFM within the LES framework is nearly independent of the flame filter size Δ. As the mesh is coarsened and Δ increases, the resolved flame surface decreases, while the corresponding subgrid-scale contribution increases. These compensating effects

Table 3
Models description adopted in the simulations.

Description	Models and mechinisms
Turbulence	RNG $k-\varepsilon$ [21] and LES Smagorinsky [22]
Wall heat transfer	GruMO-UniMORE [23]
Near wall treatment	Standard wall function
Combustion model	ECFM SB [24]
Ignition model	ISSIM [25]
Kinetic mechanism	Stagni et al. [26]

Table 4
Mesh strategy adopted for RANS and LES framework.

Mesh Description	Mesh size
Base Size Mesh	4.0 mm
Cylinder Mesh RANS	1.0 mm
Cylinder Mesh LES	0.5 mm
Main Fixed Embeddings	
Spark Ref.	0.125 mm
Intake-Exhaust Valves	0.5 mm
Adaptive Mesh Refinement	
Velocity	0.5 mm
Progress variable (Flame)	0.25 mm

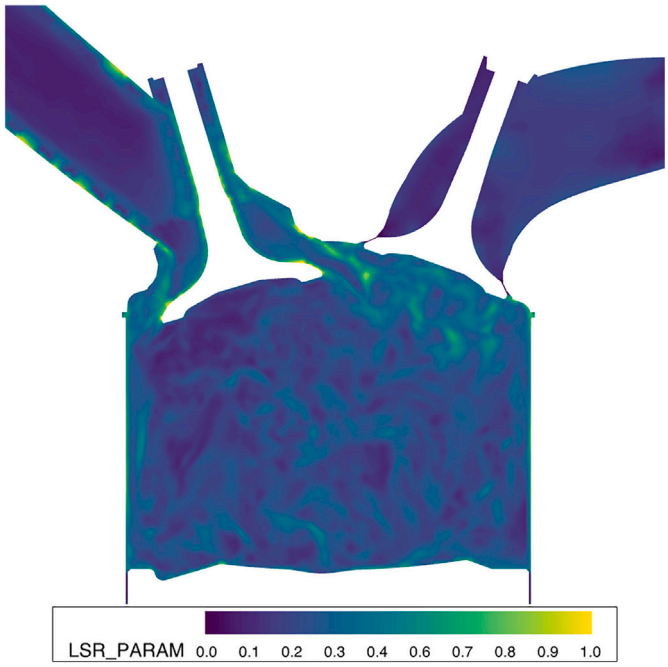


Fig. 2. LSR scalar field of the engine slice during the intake phase for an intake pressure of 1.2 bar.

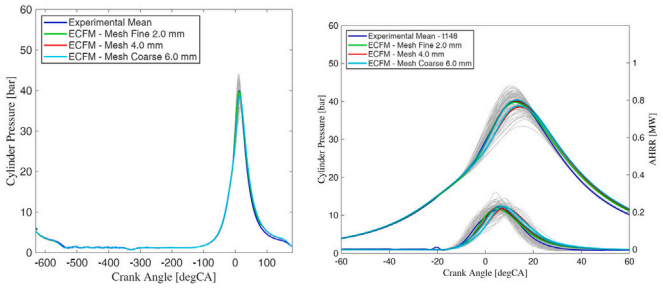


Fig. 3. Mesh sensitivity for the RANS approach testing three different base mesh sizes.

Table 5
Engine parameters for the mesh sensitivity analysis.

Mesh sensitivity	MFB 0–50 [degCA]	Peak pressure [bar]
Exp	26.0	39.9
Mesh Coarse	29.8	38.8
Mesh 4.0 mm	29.8	38.6
Mesh Fine	27.3	39.8

help ensure that the predicted combustion process remains largely independent of the mesh resolution [29].

3.2. Combustion models and calibration process

In this study, a flamelet-based combustion model was employed to numerically describe premixed flame combustion under engine-like conditions, considering different fuel mixtures and turbulence regimes. The primary objective was to assess the predictive capability of this well-established model across a range of combustion regimes. Furthermore, the present study evaluated the capability of the model to simulate ammonia–hydrogen blends in a modern internal combustion engine. Finally, the comparison between two different turbulence modelling approaches indicated whether the combustion model's performance strongly depends on the specific turbulence model adopted.

A detailed analysis was performed using ECFM, applied within both RANS and LES frameworks to examine whether consistent model behaviour is preserved when changing the turbulence modelling approach. In particular, the present work aims to isolate the effect of the turbulence modelling approach and demonstrate whether the limited predictive capability of the combustion model under investigation is primarily related to the turbulence description or with intrinsic limitations of the combustion model itself. Turbulence quantities constitute one of the primary inputs to flamelet-based combustion models; therefore, assessing the influence of different turbulence closures on model performance is essential for evaluating the predictive capability of the combustion model.

The species-based ECFM formulation [24] is fully implemented in the CONVERGE code and relies on a detailed representation of flame-turbulence interaction through the transport equation of the flame surface density (Σ). Flame propagation is also governed by the laminar flame speed, which is provided as an input to the model. The laminar flame speed depends on the fuel properties and the thermodynamic conditions inside the combustion chamber, including fuel composition, temperature, pressure, and residual gas fraction. More specifically, the laminar flame speed look-up tables were generated by discretising the relevant ranges of pressure, temperature, and equivalence ratio. The 1D simulations covered pressures from 3 to 80 bar, temperatures from 400 to 1500 K, and equivalence ratios from 0.5 to 1.3. Laminar flame speed look-up tables were generated using the Chemistry tool in the CONVERGE code for all fuel mixtures investigated in the engine. The tables were computed using the kinetic mechanism developed by Stagni et al. [26], which describes the oxidation of ammonia–hydrogen blends under low- and intermediate-temperature conditions, including diluted environments, and consists of 31 species and 203 reactions. The kinetic mechanism was selected based on its demonstrated reliability in predicting laminar burning velocities, as validated against experimental data [30,31]. Therefore, significant differences in the predicted combustion behaviour are not expected when using alternative kinetic mechanisms that exhibit similarly low errors in laminar flame speed predictions relative to the experimental data.

In ECFM, both turbulence and chemical effects contribute to defining the consumption rate of species in the unburned mixture within a simplified chemistry framework, without the need to solve transport equations for all intermediate species and radicals involved in the combustion process. The species consumption rate is represented by the source term $\dot{\omega}$ in Eq. (1). The formulation depends on the unstretched laminar flame speed, S_l^0, extracted from the chemistry table, and contributes to the transport equations governing the species participating in the combustion process.

$$\tilde{\omega}_c^{\Sigma} = \frac{\rho_u}{\bar{\rho}} S_l^0 \tilde{\Sigma} \tag{1}$$

The primary focus is placed on the transport equation of the flame surface density, Σ, as it represents the key factor through which the combustion model predicts variations in flame development arising from turbulence and flame instability phenomena. The Σ transport equation, given by Eq. (2), is defined locally and comprises several source terms. The overall structure of the transport equation is retained in both the RANS and LES frameworks, while the detailed formulation of some source terms differs to account for the different turbulence descriptions and, in particular, the corresponding estimation of u' and l_t. The relevant differences between the RANS and LES formulations are briefly discussed in this section.

$$\frac{\partial \Sigma}{\partial t} + \frac{\partial \left(u_i \Sigma\right)}{\partial x_i} = \frac{\partial}{\partial x_i}\left(\frac{\mu}{\mathrm{Sc}} \frac{\partial}{\partial x_i}\left(\frac{\Sigma}{\bar{\rho}}\right)\right) + \left(A_{t,\mathrm{sgs}} + A_{t,\mathrm{res}} + \mathrm{Curv}_{\mathrm{sgs}} + \mathrm{Curv}_{\mathrm{res}}\right)\Sigma - D + P_k \tag{2}$$

Omitting the classical terms accounting for unsteady, convection, and diffusion phenomena, the analysis focuses on the source and sink terms, which are modelled as follows in the RANS layout:

- $A_{t,\mathrm{sgs}} = \alpha K_t$ represents the flame surface production due to turbulent strain from the subgrid-scale contribution of the velocity field.
- $A_{t,\mathrm{res}} = \frac{2}{3}\frac{\partial \tilde{u}_i}{\partial x_i}$ accounts for the strain contribution from the resolved part of the velocity field.
- $\mathrm{Curv}_{\mathrm{sgs}} = \frac{2}{3}\frac{\rho_u}{\rho_b} S_l \frac{1-\tilde{c}_\Sigma}{\tilde{c}} \Sigma$ represents flame stretch due to curvature arising from the subgrid-scale contribution. $\tilde{c}_\Sigma$ represents the actual progress variable, except in the presence of autoignition phenomena.
- For the RANS formulation of the combustion model, the resolved curvature is null.
- $D = \beta S_l \frac{\Sigma^2}{1-\tilde{c}}$ represents the remaining component of flame stretch due to curvature of the flame front.
- $\mathrm{P_k}$ is a source term representing the contribution from spark ignition based on the ISSIM model [25].

In the Discussion section, each source term is analysed to better understand the combustion process and to identify the dominant contributions to flame stretch. The flame surface density quantifies flame surface wrinkling and therefore represents the contribution of turbulence to flame propagation. Several models are available to describe the turbulent strain arising from subgrid-scale contributions; in the present analysis, the most recent formulation was adopted for all simulations, both RANS and LES. In particular, the subgrid-scale turbulent strain term $A_{t,\mathrm{sgs}}$ is defined according to Eq. (3) in Suillaud et al. [32].

$$A_{t,\mathrm{sgs}} = \alpha \frac{3}{\sqrt{55}} K a \frac{S_L^0}{\delta_L}\left[1 - \exp\left(-\frac{3}{2} C_{k+} \frac{1}{\mathrm{Re}_t}\left(\frac{\pi l_t}{\delta_c}\right)^{4/3}\right)\right]^{1/2} \tag{3}$$

The efficiency function C_{k+} is modelled as a Heaviside function with a cut-off scale δ_c, such that $C(k_+) = 1$ when $k_+ < \frac{l_t}{\delta_c}$ and $C(k_+) = 0$ otherwise. This approach considers the flame as a low-pass filter (LPF) in terms of turbulence wavenumber. The cut-off scale δ_c is identified as the laminar flame thickness. This value is chosen to best reproduce the tangential strain rate observed in DNS simulations, which were used to calibrate the model closure.

In the case of LES simulations, the ECFM formulation remains largely unchanged, except for certain source terms that are adapted to account for the different resolution of the turbulence spectrum, including modified formulations for the resolved flame stretch. More specifically, both the resolved strain and curvature terms are reformulated to account for the portion of flame wrinkling that is explicitly captured by the LES approach, which is modelled as follows:

- $A_{t,\mathrm{res}}^{\mathrm{LES}} = \left(\frac{\partial \tilde{u}_i}{\partial x_i} - K_{ij}\frac{\partial \tilde{u}_i}{\partial x_j}\right)\tilde{\Sigma}$ represents the flame surface production due to turbulent strain from the resolved part of the velocity field.
- $\mathrm{Curv}_{\mathrm{res}}^{\mathrm{LES}} = S_d\left(\frac{\partial N_i}{\partial x_i}\right)\tilde{\Sigma}$ accounts for the stretch due to the curvature of the resolved part of the flame front, where S_d denotes the displacement speed approximated as $\frac{\rho_u}{\bar{\rho}} S_l$.

Nevertheless, the subgrid-scale contribution remains essential for accurately representing the overall flame wrinkling and is unchanged with respect to the RANS formulation. In the subsequent analysis, it will become clear how the LES approach differs from the RANS approach in modelling u' and l_t, which represent the fluctuating component of the velocity field and the turbulent length scale, respectively. Both quantities will be evaluated through a comparison between the two approaches. Further details on the different formulations of the ECFM for RANS and LES turbulence modelling approaches are provided in the original publications describing the model [24,29].

Regarding the calibration process, the constant α in Eq. (3) represents the only calibration parameter for both RANS and LES simulations and is used to adjust the turbulence–flame interaction by tuning the flame surface density Σ. All other parameters were kept unchanged, and the numerical setup was consistently aligned with the experimental conditions for all operating points.

3.3. Numerical validation

Before analysing the combustion results, the three-dimensional CFD model was validated against experimental data over the full engine cycle. The validation focused on verifying the trapped mass after the intake process and the effective compression ratio, which is strongly dependent on the accuracy of the valve lift profiles implemented in the CFD model. Thanks to the availability of a comprehensive experimental dataset, it was possible to validate the valve profiles and the effective compression ratio starting from the expansion stroke (90°CA). The engine was operated on a research test bench equipped with all the necessary instrumentation to accurately measure the main thermodynamic quantities. The simulations were initiated during the expansion stroke by applying the appropriate initial pressure and temperature conditions in each region, together with the corresponding boundary conditions derived from the test-bench measurements. The simulation was started prior to exhaust valve opening (EVO), enabling a detailed assessment of the valve lift profiles and validation of the imposed boundary conditions. This validation was performed by comparing the cylinder pressure oscillations predicted by the CFD model with those measured by the in-cylinder pressure transducer. The same methodology was applied to both the RANS and LES analyses, using identical initial and boundary conditions. This ensures that the two turbulence modelling approaches are subjected to the same thermodynamic and operating conditions throughout the engine cycle, allowing differences in the subsequent combustion behaviour to be primarily attributed to the adopted turbulence description rather than to differences in the imposed conditions. The consistency of the thermodynamic evolution over the full engine cycle between the two approaches further supports the validity of the subsequent comparison of their combustion behaviour. The compression ratio and trapped mass were also validated against experimental data by comparing the numerically predicted mass trapped per cycle with the mass flow rates of hydrogen, ammonia, and air measured on the test bench. Once a reliable CFD model was established for a reference operating condition, the same model configuration was shown to be applicable to all other operating cases. As shown in Fig. 4, the in-cylinder pressure predicted by the CFD model closely matches the experimental measurements over

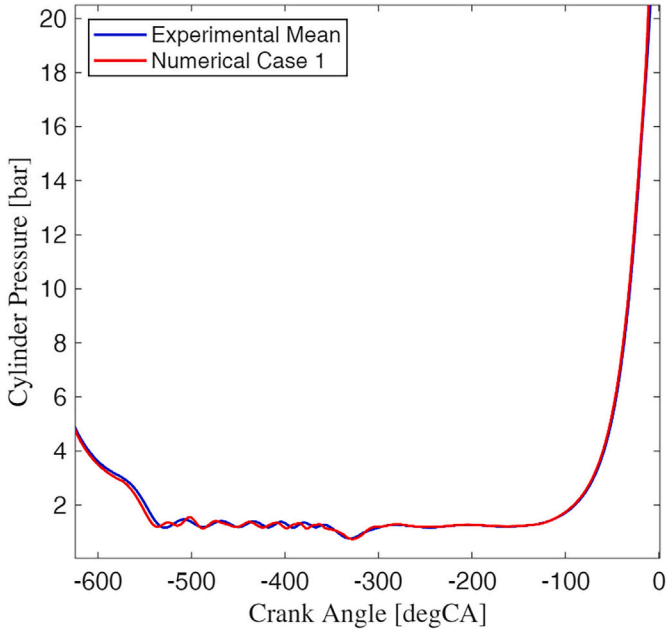


Fig. 4. Numerical–experimental correlation for the cold flow cycle (case at an intake pressure of 1.2 bar).

the entire engine cycle. In particular, the timing of the exhaust valve opening (EVO) and intake valve opening (IVO) is accurately captured. These events are identified in the figure by the characteristic pressure drops, occurring respectively shortly after −600°CA for EVO and just before −300°CA for IVO. A relevant blow-by phenomenon was identified by comparing motored-cycle validation results with the corresponding fired-cycle simulations, which allowed assessment of leakage through the piston crevices. This effect is visible in the results analysis; however, its magnitude does not affect the conclusions of the study. Two consecutive engine cycles were simulated for all RANS calculations, whereas at least five consecutive cycles were computed for the LES cases to assess result reliability and to evaluate the COV of the numerically predicted in-cylinder pressure. Since the primary objective of this study is to assess the calibration sensitivity and predictive capability of the combustion models, this setup was considered sufficient to ensure confidence in the calibration procedure for each operating condition.

4. Results discussion

4.1. Numerical assessment of RANS predictive capability

Firstly, the RANS results will be analysed to assess the ability of the model to reproduce flame propagation for different ammonia–hydrogen mixtures while varying the equivalence ratio and intake pressure. This part constitutes the foundation of the analysis and provides the basis for the subsequent LES investigation aimed at verifying the model behaviour under the same operating conditions. Fig. 5 summarizes all the operating conditions investigated through RANS simulations at an intake pressure of 1.2 bar. This represents the highest intake pressure considered, enabling more stable combustion conditions even for lean mixtures with lower ammonia content. The red box in each case indicates the calibrated value of α used to achieve the best agreement with the experimental data. The focus of the present section is instead on the flexibility of the models when the mixture properties are varied, rather than on perfectly reproducing the combustion process for each

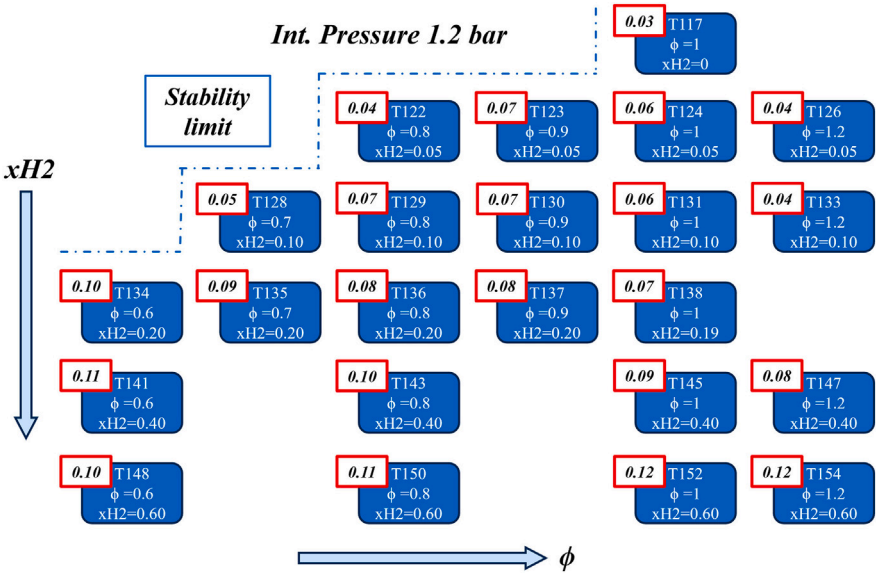


Fig. 5. Operating conditions matrix by displaying the α parameter for each case at an intake pressure of 1.2 bar.

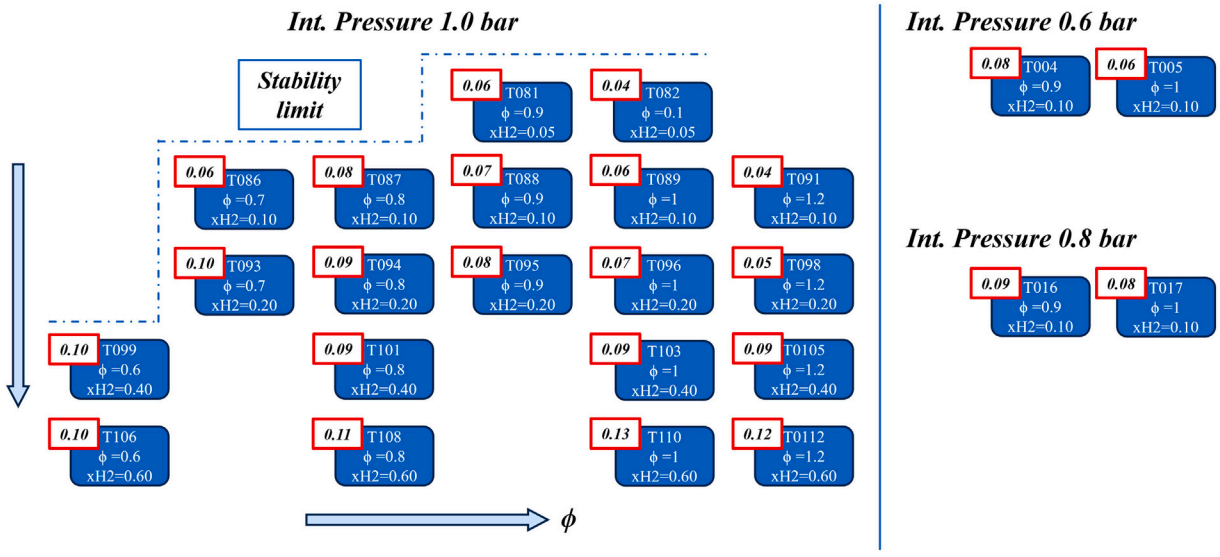


Fig. 6. Operating conditions matrix by displaying the α parameter for each case at 1.0, 0.8, and 0.6 bar of intake pressure.

case. For this reason, qualitative indicators such as the pressure traces and the Apparent Heat Release Rate (AHRR) curves were considered sufficient for the purposes of this study. Moreover, the Mass Fraction Burned (MFB) was also considered during the calibration process; however, it is not presented in this work as it would provide information largely redundant with the combustion trends already captured by the pressure and AHRR results. As shown in the figure, the mixture composition varies from top to bottom with increasing hydrogen content and from left to right with increasing equivalence ratio. Not all of the available operating points were simulated in order to reduce the overall computational cost. For example, for the mixtures containing 60% and 40% of hydrogen, some lean operating conditions were not included in the simulations. However, this does not affect the overall analysis, since the selected cases were chosen to be sufficiently and evenly distributed to allow a clear evaluation of the trends.

In order to evaluate the model performance at different intake pressures, which correspond to different engine load conditions, an additional set of simulations was analysed. Fig. 6 lists the remaining operating conditions simulated at different intake pressures in order to verify whether the same calibration trends are maintained when the intake pressure is varied. Again, the red boxes represent the α values calibrated point by point in order to match the experimental data. For all the operating points shown in the figure, an additional non-calibrated case was also simulated using a constant value of $\alpha = 0.09$. The non-calibrated cases are useful for evaluating the sensitivity to variations in α. In fact, it is important not only to determine how α should be adjusted to match the experimental data, but also to assess how the predicted combustion process changes when α is modified by a given amount. More specifically, the predictive capability of the model is directly related to its sensitivity to variations in the α parameter, which is used to compensate for modelling uncertainties in the prediction of flame stretch.

Fig. 7 shows the numerical results obtained from four cases extracted from Fig. 5, where the hydrogen content in the mixture is varied from 60% (bottom row) to pure ammonia (top row), while maintaining stoichiometric conditions. This figure is particularly effective in illustrating the range of Karlovitz numbers and the corresponding shift in combustion regimes resulting from changes in mixture properties and hydrogen concentration in the fuel. The Borghi-Peters diagram is used for a qualitative analysis to evaluate the relative shift in combustion regimes among the analysed cases. In particular, the curve is coloured according to the crank angle, from −50° CA up to 40° CA after top dead centre (TDC), by which point the combustion process is approximately completed. Moreover, the curve represents the mean value evaluated over the entire flame front in order to improve clarity and highlight the evolution of the combustion process. Starting the analysis from the Borghi-Peters diagram, it is clear that by reducing the hydrogen content in the fuel the combustion process shifts from a strictly corrugated and wrinkled flame structure, typically described by the flamelet assumption, towards the thin reaction zone, approaching the $Ka = 100$ threshold. In particular, for the stoichiometric pure ammonia case, it is evident that during the early phase of the combustion process the relatively low reactivity of the mixture, combined with the early spark timing (for case t117 at −50° CA), corresponding to very low temperature conditions, leads to high Karlovitz numbers located approximately in the middle of the thin reaction zone regime. On the other hand, the highest reactivity case (t152) shows a markedly different combustion behaviour, with a spark ignition at −13° CA, which is more representative of typical fuel mixtures used in conventional internal combustion engines. In this case, the higher hydrogen concentration compensates for the low reactivity of ammonia by increasing the laminar flame speed and consequently reducing the laminar flame thickness.

On the left side of Fig. 7, the numerical results, including in-cylinder pressure and AHRR, are presented. In detail, three curves are shown for each case. The blue curve represents the mean of the 100 experimental cycles, while the grey cloud in the background illustrates

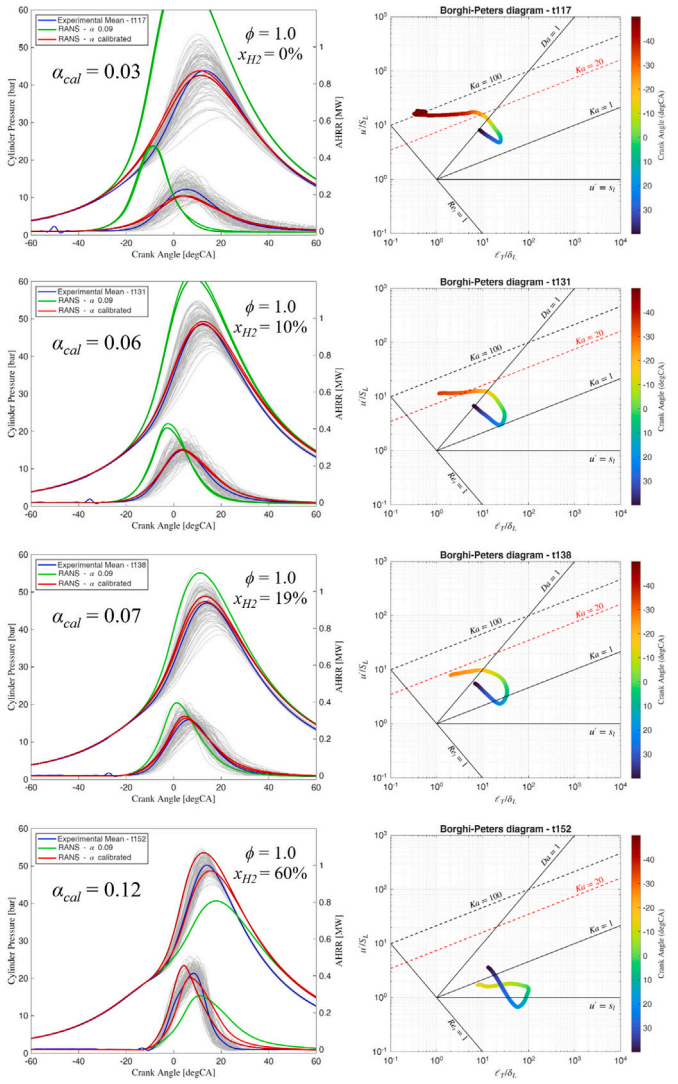


Fig. 7. Numerical results obtained by varying the hydrogen content in the mixture. On the left, in-cylinder pressure and AHRR comparisons between calibrated and non-calibrated cases are shown. On the right, the corresponding Borghi–Peters diagram is reported for each case.

the cycle-to-cycle variability of these measurements. The numerical results are displayed in green and red. The red curve represents the RANS–ECFM simulation calibrated through the α parameter, whereas the green curve corresponds to the non-calibrated numerical case obtained using a constant value of $\alpha = 0.09$. The ability of the ECFM model to reproduce the combustion process by calibrating the turbulence interaction is well established in the literature, and the present results confirm this capability even for alternative fuel blends such as those considered in this dataset. The only case where the model shows some difficulty in matching the experimental heat release is the pure ammonia case, particularly during the early phase of the combustion process, which is strongly influenced by high Karlovitz number conditions. In fact, while the model effectively reproduces the combustion propagation in all the other cases by selecting an appropriate α value, the pure ammonia case exhibits a significant shift in combustion regime from the initial phase to the main part of the combustion process, resulting in a non-perfect match between the numerical red curve and the experimental mean curve. The green numerical curve illustrates the sensitivity of the model when a single calibration parameter is used for all operating points. In this case, significant errors appear in the prediction of flame

propagation and heat release for almost all cases, highlighting a key issue particularly relevant for mixtures with low hydrogen content. In the plots, the calibrated α parameter is included to highlight the trend observed when reducing the hydrogen content. The same type of analysis can be performed by varying the equivalence ratio while keeping the hydrogen concentration constant.

In Fig. 8, four cases are presented, corresponding to variations in the equivalence ratio at a fixed hydrogen concentration of 10% in the fuel mixture. With respect to the Borghi–Peters diagram, the effect observed when reducing the hydrogen content is comparable to that obtained by moving towards leaner mixtures while maintaining the same hydrogen fraction. In fact, since the engine speed remains constant across all cases, the turbulence intensity is also nearly unchanged, as it depends mainly on the selected intake pressure. Therefore, the mixture reactivity primarily determines the Karlovitz number and, consequently, the combustion regime of the process. The numerical curves and the corresponding α values illustrate the model behaviour for lean ammonia–hydrogen blends. Focusing on the fuel mixture with 10% x_{H_2}, it is evident that the model performs well under stoichiometric conditions and up to $\phi = 0.8$. However, a decrease in predictive capability is observed for the leanest condition, which corresponds to the highest Karlovitz number, similarly to what was discussed in the previous stoichiometric analysis. The non-calibrated case confirms that the relative error remains almost constant from stoichiometric conditions up to $\phi = 0.8$, while showing a higher relative error at the leanest operating point.

Overall, Figs. 9 and 10 show the α trends as a function of equivalence ratio and hydrogen content, including all the operating points defined in the matrix previously shown. It is straightforward to observe that, when varying the intake pressure from 1.2 bar (Fig. 9) to 1.0 bar (Fig. 10), the main calibration trends of the combustion model remain essentially unchanged. In particular, for all the fuel mixtures tested, α increases as the mixture becomes leaner, except for the 60% hydrogen case, which exhibits a slight decrease under lean conditions. On the other hand, the trend of α as a function of hydrogen content is even more evident. In fact, for both intake pressures, the calibration parameter increases with increasing hydrogen fraction. This behaviour is particularly clear when analysing the stoichiometric cases and comparing the different fuel mixtures. In both the 1.2 bar and 1.0 bar charts, the leanest cases with low hydrogen content exhibit an inversion in behaviour compared to the general calibration trend observed under lean conditions (i.e., the leanest yellow and orange cases). This behaviour is driven by the very high Karlovitz numbers reached in these extreme cases, particularly during the early phase of the combustion process. In these conditions, the very advanced spark timing leads to an unusual development of the initial flame kernel. Since the model does not include a dynamic calibration of α throughout the engine cycle, the selected value represents a compromise between accurately capturing the early flame development and the main

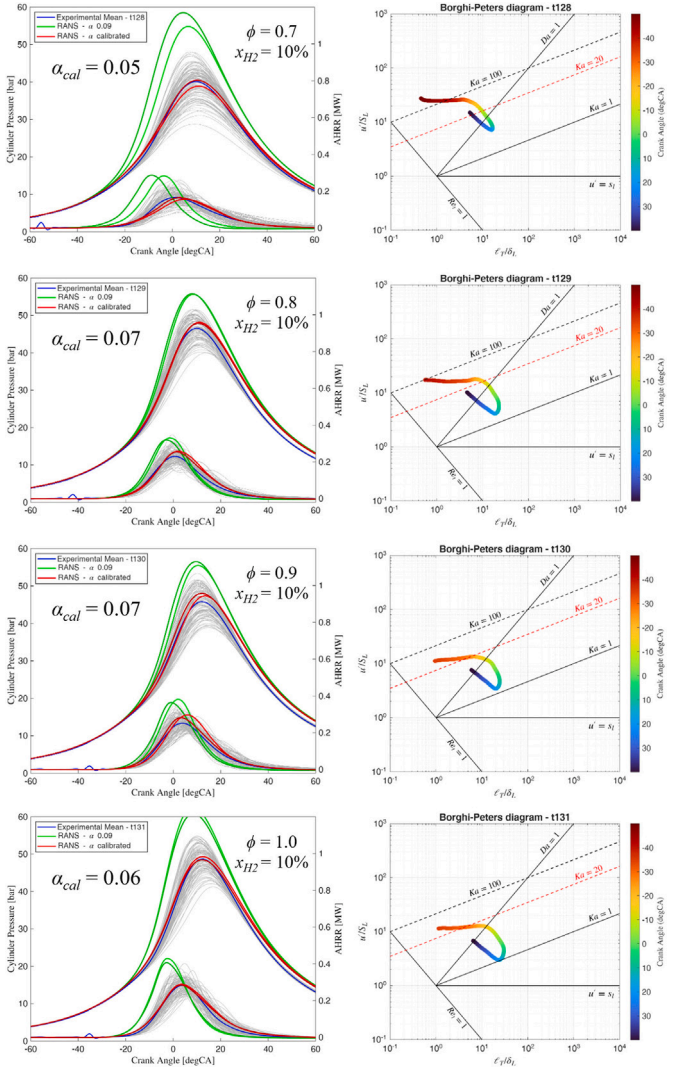


Fig. 8. Numerical results obtained by varying the equivalence ratio at a fixed hydrogen concentration of 10%.

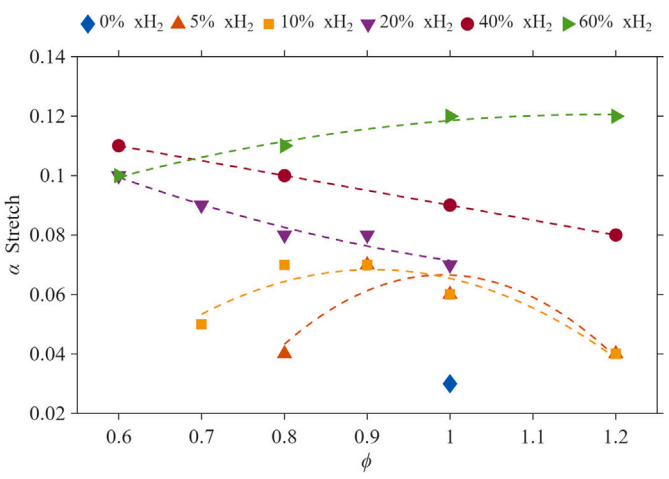


Fig. 9. Numerical trends of α variation as a function of equivalence ratio and hydrogen content at an intake pressure of 1.2 bar.

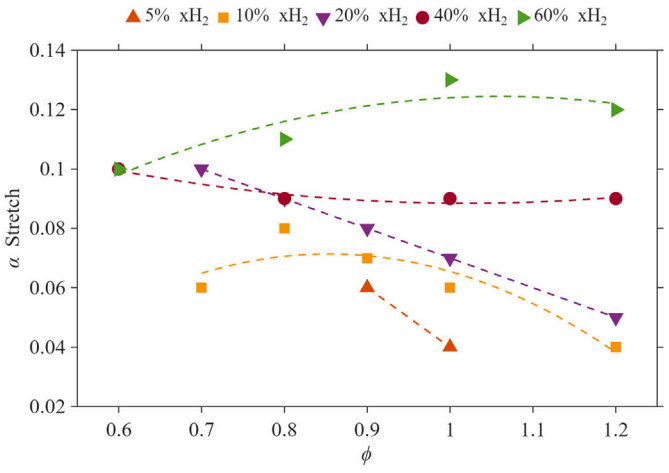


Fig. 10. Numerical trends of α variation as a function of equivalence ratio and hydrogen content at an intake pressure of 1.0 bar.

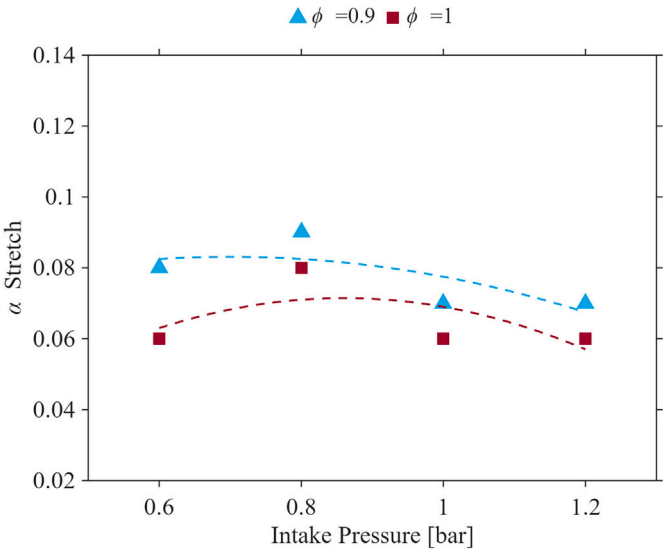


Fig. 11. Numerical trends of α variation at a fixed hydrogen content of 10% as a function of intake pressure.

combustion phase near TDC, where higher temperatures promote flame propagation. This phenomenon is especially evident in low-reactivity mixtures with low hydrogen content, which are characterized by very low laminar flame speeds. It is also worth noting that, apart from the conditions described above, the model generally exhibits a more predictive behaviour when varying the hydrogen content under lean conditions than under stoichiometric ones. This is evidenced by the trends, which tend to converge as the mixture becomes leaner. Nevertheless, the physical interpretation of the combustion model parameters remains not entirely straightforward when multiple complex phenomena occur simultaneously. It is known that, for a given fuel mixture and based on the observed behaviour of the ECFM model, the turbulent flame speed tends to be overestimated as the Karlovitz number increases. Consequently, in very high Karlovitz number conditions, a reduction of the α value is required in order to compensate for this overprediction of the turbulent flame speed. This effect is particularly relevant for the stoichiometric cases, for which thermo-diffusive effects are not expected to play a significant role. Indeed, varying the hydrogen content of the fuel while maintaining a stoichiometric mixture provides a clearer indication of the effect of increasing the Karlovitz number on the flame structure and flame-turbulence interaction. In this case, the observed variations in the calibrated α parameter can therefore be primarily associated with changes in the combustion regime induced by the different hydrogen contents, rather than with thermo-diffusive flame instabilities. On the other hand, by varying the intake pressure while maintaining the same equivalence ratio and hydrogen content in the fuel, the trends of α can again be observed for the same mixture composition (10% x_{H_2}) and for two equivalence ratios (0.9 and 1.0). Fig. 11 clearly shows that the α calibration does not vary significantly when changing the load through variations in intake pressure, while maintaining the same fuel mixture properties.

4.2. Numerical assessment of LES predictive capability

This section first presents the numerical results obtained using the LES turbulence model, with the aim of verifying whether the combustion model maintains consistent behaviour when the operating conditions are varied. In a second phase, a more detailed analysis of the individual flame stretch source terms is carried out, and RANS and LES results are compared. The aim of this discussion is to assess whether the same combustion model exhibits consistent calibration trends when a different turbulence approach, providing a more resolved flow field, is employed. Due to the higher computational cost associated with the LES approach, only a subset of the previously defined operating conditions was selected to evaluate the model behaviour. For each condition, simulations were performed over five consecutive engine cycles to assess the robustness and consistency of the combustion model calibration in reproducing the corresponding experimental data. The calibrated results were subsequently evaluated using quantitative error metrics based on relevant engine parameters, including the MFB 0–50% interval and the peak cylinder pressure. These metrics were used to assess the consistency of the calibration across the simulated cycles and to provide a quantitative measure of the agreement between the numerical and experimental results. The authors acknowledge that five consecutive LES cycles are not sufficient to provide a statistically robust characterization of cycle-to-cycle variability, which would require a substantially larger number of cycles and, consequently, significantly higher computational cost. Nevertheless, the five-cycle simulations are considered sufficient for the present objective, which is to assess the consistency and robustness of the combustion model calibration rather than to characterize the full statistical distribution of cycle-to-cycle variability. Consistent with the RANS approach, the LES simulations were calibrated using the same α parameter, which adjusts the flame stretch contribution associated with the subgrid-scale strain rate in the flame surface density formulation. Fig. 12 presents the LES numerical results, which are compared with the corresponding RANS results for the 1.2 bar case. Similarly, the same mixture conditions were selected in order to assess the model adaptability under 1.0 bar of intake pressure. In total, nine cases were simulated using LES (t152, t148, t131, t128, and t117 at 1.2 bar, along with the corresponding cases at 1.0 bar), with the aim of covering the most representative and extreme conditions in terms of α calibration previously identified in the RANS analysis. The green curves represent the two cycles obtained using the RANS model, whereas the five red curves, displayed with progressively darker shades, correspond to the five LES cycles computed for each condition. In particular, the lightest red shade represents the first

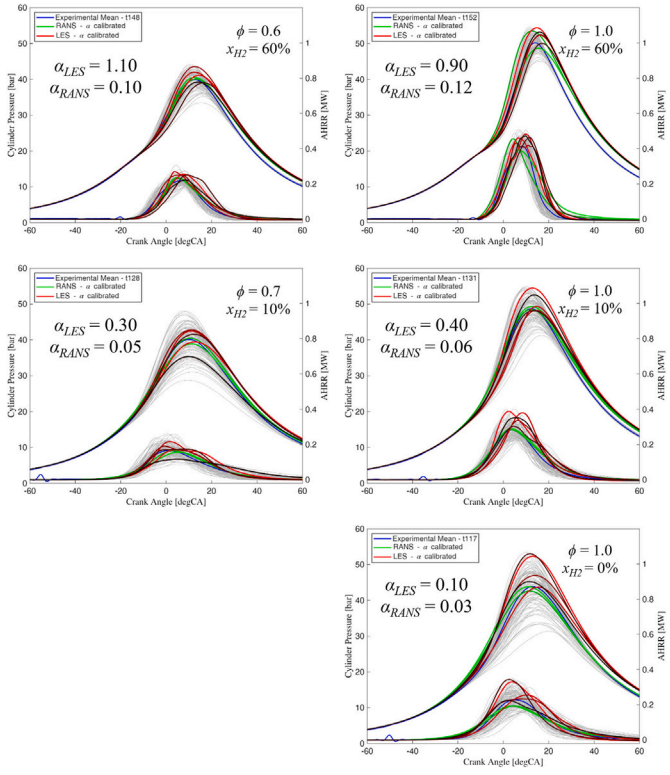


Fig. 12. LES numerical results are compared with RANS results at an intake pressure of 1.2 bar.

cycle, while the subsequent cycles are shown with increasingly darker tones to clearly highlight the cycle-to-cycle variability.

As previously demonstrated with the RANS results, the LES approach confirms that the same combustion model is able to reproduce the combustion process with good accuracy when calibrated point-to-point using a single parameter. On the other hand, consistent with the RANS findings, the model requires significant recalibration when the hydrogen content is varied. A more robust predictive capability is observed when varying the equivalence ratio from stoichiometric to lean conditions, for both high and low hydrogen content mixtures. These trends are further confirmed by the relative variation of the α parameter expressed as a percentage. Figs. 13 and 14 show the relative variation of α, normalized by the case with the highest α value, for both RANS and LES simulations. The legend indicates the hydrogen content in the fuel (expressed as a percentage) as well as the turbulence modelling approach. Hollow symbols correspond to LES results, whereas filled symbols represent RANS results. The colour coding identifies the fuel composition: green corresponds to 60% hydrogen content, red to 10%, and blue to pure ammonia mixtures. These charts provide a clear representation of the combustion model performance as a function of hydrogen content and equivalence ratio. Moreover, they confirm that the model exhibits consistent behaviour across both RANS and LES turbulence approaches, and that the need for recalibration when varying the hydrogen content persists even with a more resolved description of turbulence. More specifically, as previously discussed, decreasing the hydrogen concentration requires a reduction of the α parameter in order to compensate for the overestimation of flame stretch in high Karlovitz number regimes. This behaviour is consistently observed for both 1.2 bar and 1.0 bar intake pressure conditions. This behaviour could be partially attributed to uncertainties in the kinetic mechanisms when varying the hydrogen content. However, it is reasonable to assume that the magnitude of these deviations cannot be explained by uncertainties in the laminar flame speed alone. It is also evident from the figures that variations in the equivalence ratio are well captured by the combustion model, without the need for extensive calibration. It is worth noting that the current ECFM formulation, in both RANS and LES layouts, does not account for thermo-diffusive effects arising from preferential diffusion in lean mixtures. This limitation is particularly relevant for hydrogen and ammonia/hydrogen mixtures, for which non-negligible thermo-diffusive effects have been reported in the literature, resulting in stretch factors greater than unity under engine conditions. However, focusing the analysis on stoichiometric mixtures, for which the flames are expected to be stable from a thermo-diffusive standpoint, provides a clearer assessment of the model behaviour as the combustion regime changes due to variations in fuel reactivity. In contrast, the non-monotonic trends observed when varying the equivalence ratio are likely influenced by the preferential-diffusion characteristics of the individual mixtures. Accurately capturing these effects would therefore require an additional model capable of dynamically predicting the stretch factor I_0 as a function of the mixture composition and thermodynamic conditions.

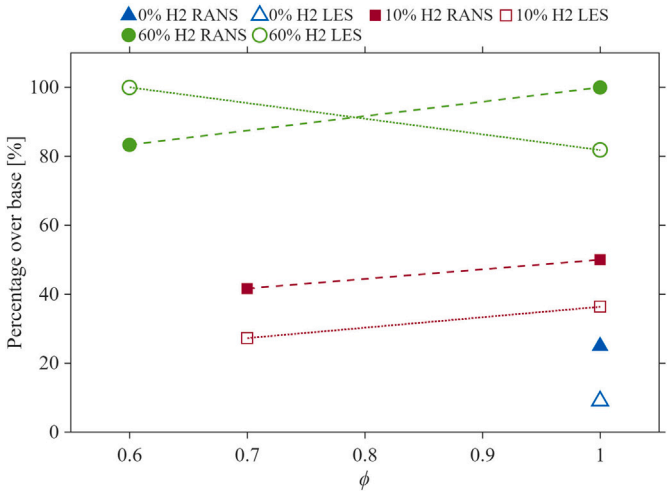


Fig. 13. Comparison of LES and RANS α trends, normalized by the case with the highest α value at an intake pressure of 1.2 bar.

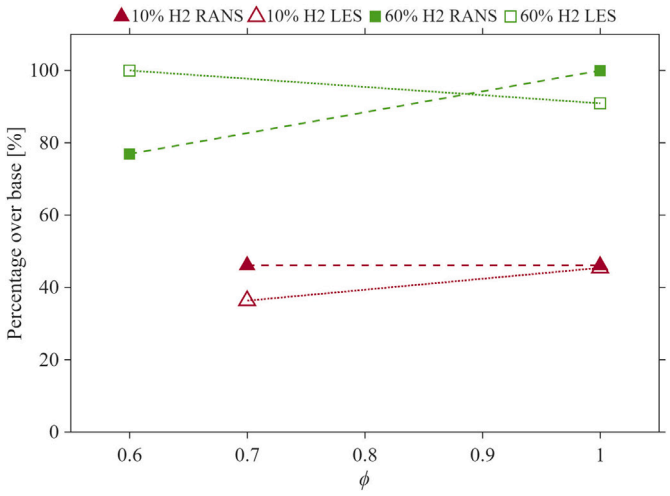


Fig. 14. Comparison of LES and RANS α trends, normalized by the case with the highest α value at an intake pressure of 1.0 bar.

Before proceeding with a more detailed analysis of the combustion model using both LES and RANS approaches, selected error metrics are introduced to strengthen the analysis and assess the actual accuracy of the model in predicting the combustion process. The error analysis is presented only for the cases at an intake pressure of 1.2 bar, as similar trends and conclusions are observed under other conditions.

To evaluate the combustion development during the main phase of the process, specific combustion parameters were selected to establish a correlation between experimental and numerical results, considering both LES and RANS simulations. Fig. 15 shows the correlation plot for

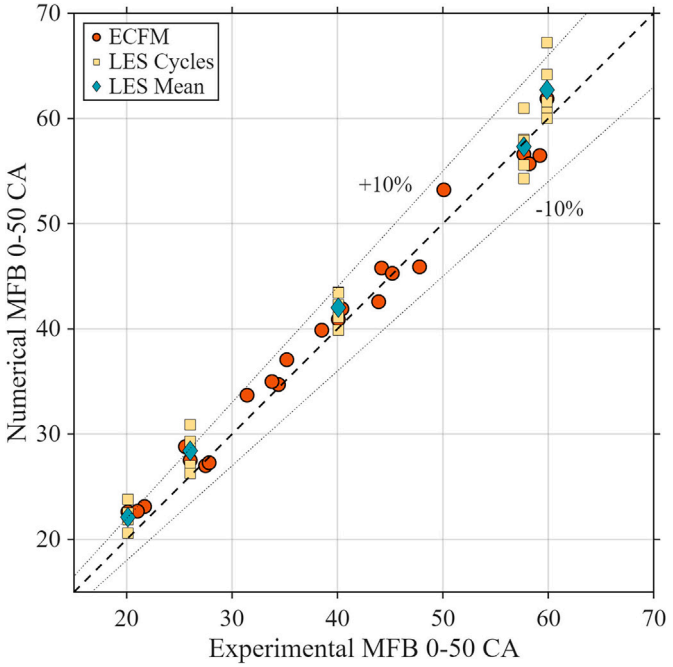


Fig. 15. Correlation plot of combustion duration (MFB 0–50) comparing RANS and LES results.

combustion duration, defined by MFB 0–50, including all LES cycles (yellow square symbols), their corresponding mean values (aqua-green symbols), and the RANS results (orange circular symbols). In terms of combustion characterization, MFB 0–50 was shown to better represent the actual behaviour of the combustion model in predicting the combustion process, without being significantly affected by secondary effects such as wall interaction or blow-by phenomena. The figure shows good agreement between the experimental data and the numerical results for both RANS and LES approaches. This is further confirmed by the computed RMSE values (defined as RMSE = $\sqrt{\frac{1}{N}\sum_{i=1}^{N}\left(y_i^{\mathrm{num}} - y_i^{\mathrm{exp}}\right)^2}$), with $RMSE_{RANS} = 1.813°CA$ and $RMSE_{LES} = 2.067°CA$, evaluated between the numerical results and the experimental mean values. It is also evident that all operating points analysed with the LES approach fall within the dotted lines representing the ±10% deviation from the experimental data. This confirms that the calibration is reliable and that the analysis is consistent with the obtained numerical results.

To further strengthen the analysis, two additional combustion parameters were selected and analysed in order to better assess the combustion model's performance and calibration. In particular, the in-cylinder peak pressure and the corresponding crank angle at peak pressure provide further insight into the model performance when comparing the two turbulence approaches. Figs. 16 and 17 show the error distribution, distinguishing between the two turbulence modelling approaches and reporting each individual cycle in the case of the LES results. By comparing the mean values for both LES and RANS results, it is evident that the combustion model accurately predicts the combustion process for both turbulence approaches, confirming the reliability of the calibration procedure. The figure adopts the same colour scheme as the correlation plot for MFB 0–50, while the red line inside each box represents the median of the error distribution. The boxes define the 25th–75th percentile range, whereas the dashed whiskers indicate the spread of the data. This analysis methodology differs from the combustion duration correlation plot due to the different nature of the data, which requires alternative approaches to properly assess the reliability of the combustion model. Nevertheless, the error distributions for both peak pressure and the corresponding crank angle consistently highlight the model's reliability across a wide range of operating conditions and mixture compositions. This analysis supports the conclusion that the calibration requirement of the combustion model primarily arises from the need to correctly represent turbulence–flame interaction, through the adjustment of the total flame stretch during propagation.

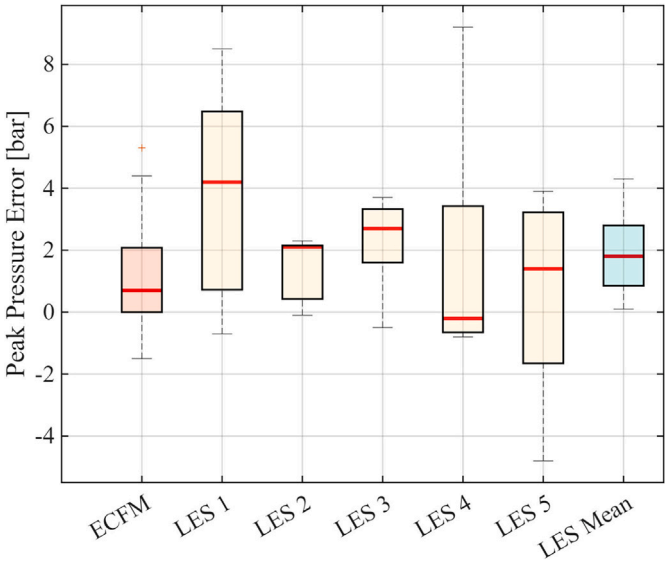


Fig. 16. Peak pressure error distribution comparing LES and RANS numerical results. For LES, both individual cycles and cycle-averaged values are reported.

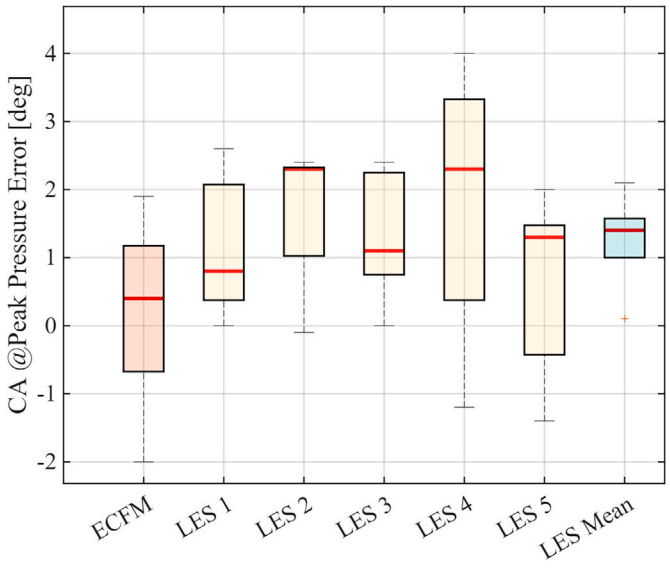


Fig. 17. Error distribution of the crank angle corresponding to the peak pressure, comparing LES and RANS numerical results.

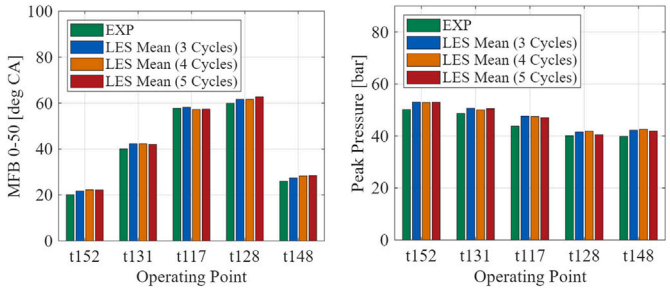


Fig. 18. Cycle-averaged MFB 0–50 and peak cylinder pressure after 3, 4, and 5 consecutive LES cycles.

More specifically, the LES mean values represent the arithmetic mean of the five simulated cycles and should not be interpreted as statistically converged cycle-averaged results, as the number of simulated cycles is not sufficient to provide a statistically robust characterization of cycle-to-cycle variability. Fig. 18 shows both the MFB 0–50 interval and the peak cylinder pressure for each operating point investigated using the LES approach, in order to assess the variation of the mean values as the number of simulated cycles increases. In particular, the mean values calculated after three, four, and five consecutive cycles are compared with the corresponding experimental results, which represent the average over the 100 experimental cycles acquired on the test bench. Although this comparison cannot be considered evidence of statistical convergence, the results show a relatively stable behaviour of the mean values as additional cycles are included. The limited variation observed between the three-, four-, and five-cycle means is considered sufficiently representative for the specific objective of the present study and provides a reasonable compromise between the consistency of the LES assessment and the substantial computational cost associated with simulating additional cycles.

4.3. Stretch source term analysis in RANS and LES frameworks

Having extensively evaluated the predictive capability of the ECFM model by varying hydrogen content, equivalence ratio, and intake pressure, and by assessing the error of the numerical results against experimental measurements, this section provides a more detailed analysis

of the model behaviour, with particular focus on the transition from the RANS to the LES framework. The objective is to examine in detail each source term contributing to the flame stretch prediction, which represents the core of the turbulence–chemistry interaction and ultimately determines the model's predictive performance.

This analysis is presented for a single operating condition; however, the same trends and conclusions are consistently observed across all other cases. In particular, the following results refer to the operating condition characterized by 60% hydrogen content ($x_{H_2} = 0.6$) and an equivalence ratio of $\phi = 0.6$, and compare the raw LES CFD data, obtained directly from the combustion model output, with the corresponding RANS results. These quantities are evaluated progressively during the combustion process as the flame propagates within the chamber. The analysis is performed by tracking the flame region and computing averaged values only within the flame front, where these terms actively influence flame propagation. The flame region is identified based on the progress variable, considering values between 0.0001 and 0.999. This criterion restricts the analysis to the active combustion zone and is consistent with the flamelet-based assumption that combustion progresses according to the local completion of fuel consumption. The validity of this approach is assessed by examining the Karlovitz number in each cell included within the selected progress-variable range. Despite the cell-to-cell dispersion, the resulting values exhibit a coherent overall Karlovitz-number level. For the LES data, all five cycles are reported to highlight the cycle-to-cycle variability effect on the combustion model.

In Fig. 19, the flame stretch induced by strain is presented by separating the subgrid-scale contribution, defined in Eq. (3), from the resolved-field component, as previously introduced in Eq. (2). In detail, the blue curve corresponds to the RANS result, while the red dashed curves represent the first four LES cycles and the solid red curve corresponds to the fifth LES cycle. Focusing on the strain contribution to the flame stretch, it is evident that the subgrid-scale component ($A_{t,sgs}$) exhibits higher values in the LES results compared to the RANS predictions. This difference is primarily associated with limitations of the model, as the uncertainties and lack of predictive capability are compensated through the calibration of the α parameter included in the LPF formulation. More specifically, the LPF formulation relies on the modelling of both u' and l_t, which are used as input parameters to predict the turbulent strain-induced flame stretch when varying fuel mixture properties. Later in this section, the differences in these input parameters between LES and RANS simulations will be analysed in detail. The different α values obtained from RANS and LES are partially attributed to the two different approaches used to estimate u' and l_t. Nevertheless, the calibration of $A_{t,sgs}$ plays a key role in adjusting the overall flame stretch, compensating for discrepancies arising from other contributions, particularly the curvature-induced stretch term. Since LES resolves a larger portion of the turbulent field compared to RANS, the subgrid-scale contribution is, in principle, expected to be higher in RANS than in LES. To clarify this aspect, the right-hand plot of Fig. 19 shows the resolved contribution to the strain-induced flame stretch for both RANS and LES results. As expected, the LES approach yields higher values than RANS due to its more resolved representation of the turbulent field.

The total flame stretch results from the combined contributions of strain and curvature, as is well established in the literature [33]. Figs. 20 and 21 present the curvature contribution by first separating the resolved and subgrid-scale components of the stretch. In a second step, the subgrid-scale contribution is further separated into its positive and negative components. The overall subgrid-scale contribution to the curvature-induced flame stretch is shown in the right-hand plot of Fig. 20, which highlights a positive contribution during the early phase of combustion and a negative contribution during the main and final stages of the process. It is worth noting that the calibration procedure does not directly affect the curvature contribution, but only the strain-related stretch. It is also evident that LES results exhibit more pronounced negative stretch values, which are compensated by the higher strain-induced stretch previously discussed. Moreover, the resolved contribution to the curvature-induced stretch appears to be relatively small compared to the subgrid-scale component. Fig. 21 further illustrates the distribution of the positive and negative subgrid-scale contributions to the curvature-induced stretch for both LES and RANS results. In particular, the Curv_{sgs} and D represent the positive and negative contributions, respectively, to the overall subgrid-scale curvature term, which is given by their combined effect. It is evident that the RANS subgrid-scale curvature contribution exhibits lower values in magnitude compared to the LES results. This leads to a reduction of α in order to calibrate $A_{t,sgs}$ and compensate for the different curvature-induced stretch contribution. Theoretically, as previously discussed, LES simulations are expected to exhibit a larger resolved flame stretch contribution, while RANS simulations should account for a larger fraction of the stretch through the subgrid-scale formulation. Consequently, both approaches are expected to provide comparable total contributions from strain and curvature by evaluating the combined terms $A_{t,sgs} + A_{t,res}$ and $\mathrm{Curv}_{sgs} + \mathrm{Curv}_{res}$. The modelling of curvature-induced stretch becomes particularly relevant in high Karlovitz regimes [34].

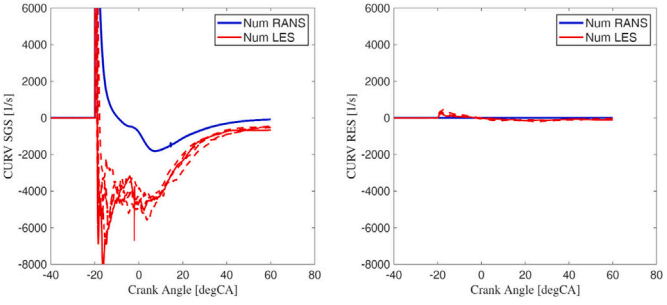


Fig. 20. Flame stretch due to curvature (CURV), decomposed into subgrid-scale (left) and resolved contributions (right), as defined in Eq. (2).

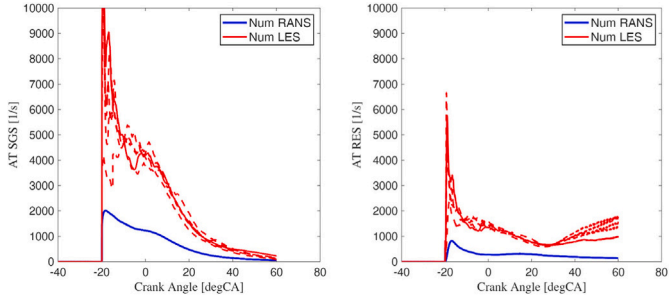


Fig. 19. Flame stretch due to the strain (At) divided into a subgrid-scale part (left) and a resolved part (right).

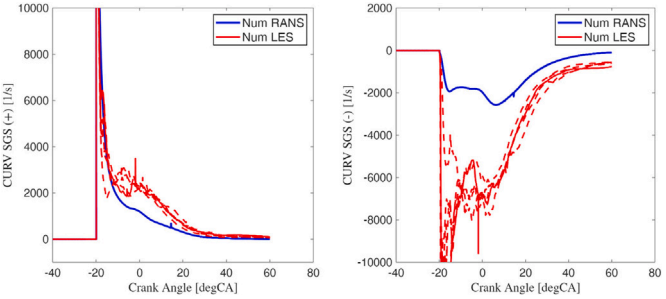


Fig. 21. Flame stretch due to the curvature by distinguishing negative subgrid-scale part (right) from the positive subgrid-scale part (left).

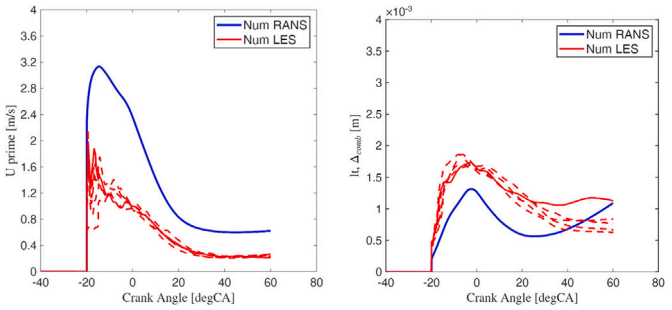


Fig. 22. Mean values of u' (left) and l_t (right) evaluated across the flame during the combustion process.

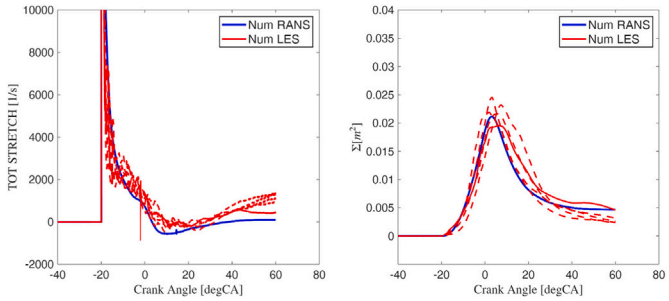


Fig. 23. Total flame stretch (left) and flame surface density Σ (right) evaluated across the flame during the combustion process.

To conclude the analysis, Fig. 22 presents two key turbulence variables influencing the subgrid-scale contribution to the flame stretch. In particular, the right-hand plot compares the turbulent velocity fluctuation u' obtained from LES and RANS for the same operating condition (t148). The two turbulence modelling approaches employ different methodologies to estimate the turbulent velocity fluctuations. In the $k-\varepsilon$ RANS framework, u' is modelled from the transport equation of turbulent kinetic energy k. Conversely, in the LES framework, u' is evaluated from the resolved velocity field according to Eq. (4) [35]:

$$u'_{\Delta,\mathrm{LES}} = c_2 \Delta_x^3 \mid \nabla^2 (\nabla \times \tilde{u}) \mid \left(\frac{\Delta}{n_x \Delta_x} \right)^2 \tag{4}$$

where $c_2 = 2$ and $n_x = 10$.

As previously discussed, the RANS approach leads to higher subgrid-scale contributions, as only the mean turbulent field is resolved. In contrast, the LES approach resolves a portion of the turbulence spectrum, resulting in lower modelled velocity fluctuations and a more physically representative description of the flow field. On the other hand, the left-hand plot shows the turbulent length scale trends, by comparing LES and RANS approaches. More specifically, in the RANS approach, the turbulent length scale l_t is computed from the two transport equations for turbulent kinetic energy k and the dissipation rate ε, using the formulation $l_t = C_\mu^{3/4} \frac{k^{3/2}}{\varepsilon}$. In the LES framework, a corresponding turbulent length scale is not explicitly modelled; instead, the combustion filter scale Δ_{comb} is introduced, which is theoretically expected to be smaller than, or at least comparable to, the RANS turbulent length scale. A direct comparison between the two quantities (l_t from RANS and Δ_{comb} from LES) is not strictly rigorous, as they are derived from fundamentally different approaches: the former depends on the turbulence model formulation, while the latter is directly related to the adopted mesh resolution. Therefore, the two quantities are not expected to be identical. Nevertheless, to better understand the combustion model behaviour, it is useful to analyse the trends shown in the figure, which indicate that the characteristic length scales are of the same order of magnitude for both approaches, with slightly higher values observed in the LES results compared to RANS. This difference is mainly attributed to the mesh resolution used in the LES simulations. This behaviour suggests that the LES mesh may be somewhat coarse; however, this compromise is accepted in order to limit computational cost. In the next section, additional simulations performed using a fine and uniform mesh are presented to demonstrate that, even with a constant cell size, the calibration range of the α parameter remains unchanged. Finally, Fig. 23 confirms the concepts discussed above by presenting the total flame stretch and the corresponding flame surface density values, Σ. In detail, the total flame stretch is obtained as the sum of all the individual contributions previously described, including both strain and curvature effects. The flame surface density, Σ, represents the solution of the corresponding transport equation, governing the fuel consumption rate and quantifying the level of flame wrinkling induced by turbulence. It is evident that both the total stretch and Σ values are comparable between RANS and LES approaches, indicating that the combustion model provides a consistent prediction of turbulence-induced effects and flame propagation across different turbulence modelling frameworks. This result is particularly relevant, as it demonstrates that the limitations in the predictive capability of the presented numerical results are mainly related to the adaptation of the combustion model when transitioning between different combustion regimes, rather than to the turbulence description used as input to the combustion model itself.

4.4. Mesh-related subgrid-scale contribution estimation in LES

In this section, a potential mesh-related issue is addressed by considering the same operating conditions previously analysed with the LES approach at an intake pressure of 1.2 bar. As previously described, in LES simulations, the turbulent velocity fluctuation u' is estimated based on the rotational component of the resolved velocity field [35]. This formulation, as with any other algebraic expression based on the local cell size, may introduce inconsistencies when coupled with an adaptive mesh refinement (AMR) strategy, where the mesh is dynamically adjusted by tracking the flame front. In particular, changes in mesh resolution, from coarser cells outside the flame front (0.5 mm) to finer cells within the flame region (0.25 mm), can lead to artificial variations in the computed u' field [36].

Fig. 24 shows the results for the fifth cycle using three different mesh strategies tested under the same operating condition (t148); similar trends were observed for all other conditions. The red curve represents

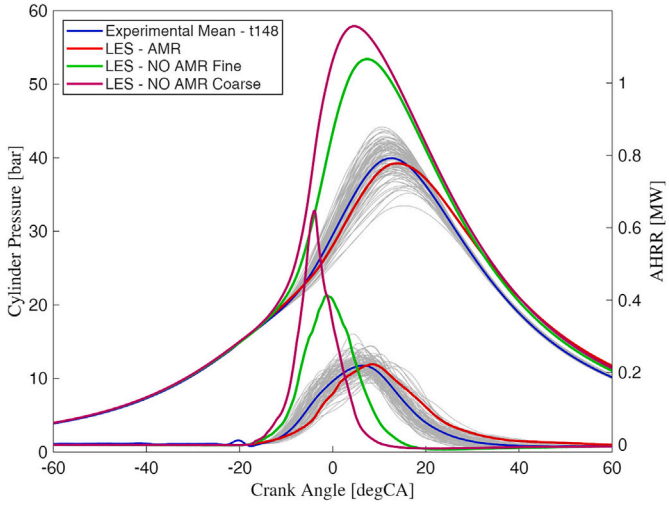


Fig. 24. Numerical results for the fifth cycle obtained with three different mesh strategies using the same α value in LES.

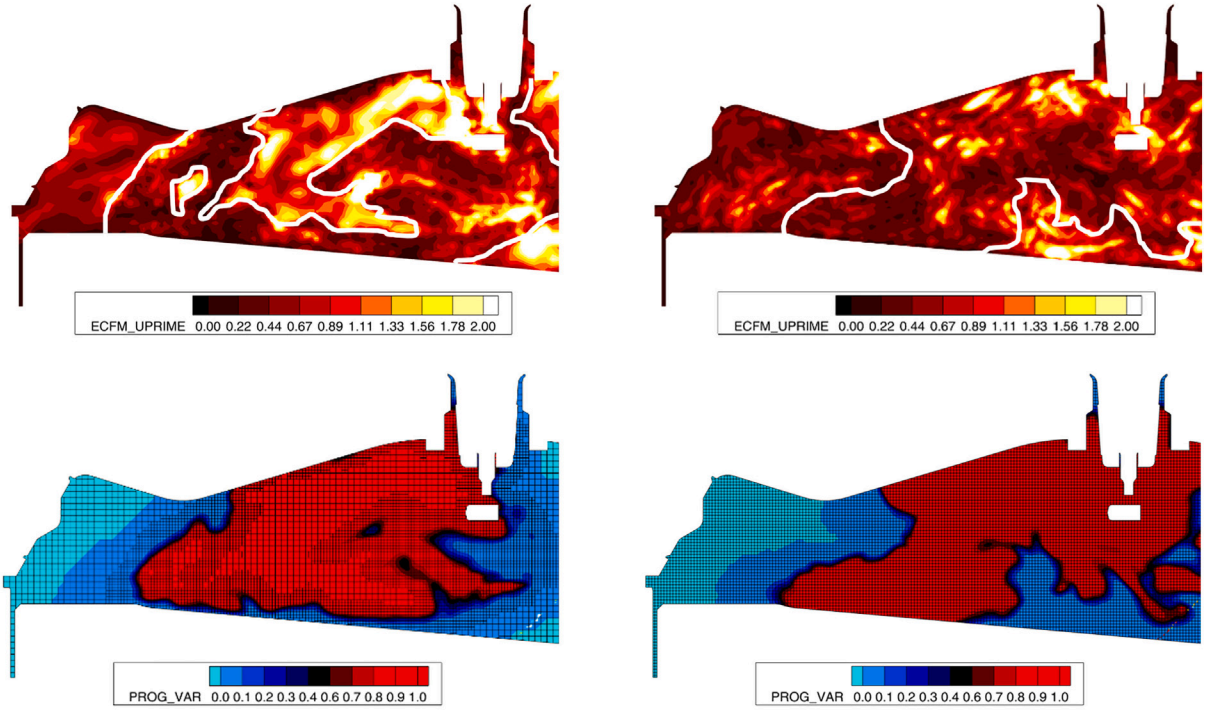


Fig. 25. Central slice of scalar fields for u' and the progress variable at TDC during combustion, comparing simulations with (left) and without (right) the AMR mesh strategy.

the standard mesh configuration used throughout the study, while the other two cases are obtained without the AMR strategy during the combustion phase. All simulations were initialized from the same initial conditions, taken from a mapping file just before the onset of combustion. The green curve corresponds to a simulation performed with a uniform mesh of 0.25 mm in the combustion chamber, whereas the pink curve represents a case with a uniform mesh of 0.5 mm. These discrepancies in in-cylinder pressure and heat release highlight the overestimation observed when using the same α parameter as in the AMR case. The differences arise primarily from the estimation of u' coupled with the AMR effect, which relies on the rotational component of the velocity field. Fig. 25 presents the three-dimensional fields for both cases: the left column shows u' and the progress variable for the simulation with AMR, while the right column corresponds to the uniform mesh case at 0.25 mm. From the u' field, a decrease in the turbulent velocity is visible at the flame front in the AMR case, caused numerically by the sudden change in mesh resolution. In the first row, the white isoline indicates the region where the mesh size changes, whereas for the uniform mesh case the isoline corresponds to the flame front location. In contrast, this behaviour is absent in the uniform mesh case (right column), where u' values remain higher across the flame. This results in faster flame propagation and heat release, solely due to the mesh configuration, without any other changes in the setup. This behaviour arises from the change in mesh resolution in front of the flame front, which prevents the rotational component of the velocity field from properly recovering the turbulent fluctuations, leading to a loss of resolved vortical structures associated with the mesh transition. Further details are provided in [36].

Fig. 26 presents a comparison of the three LES results with different mesh strategies during the combustion process, alongside the RANS result. The left-hand plot highlights the effect of AMR on the u' estimation, showing lower values of the turbulent velocity fluctuation compared to the two uniform-mesh LES results, as also illustrated by the three-dimensional engine visualizations. It is worth noting that, even without the AMR effect, all LES u' curves remain below the RANS-predicted turbulent velocity fluctuations, consistent with the previous discussion. On

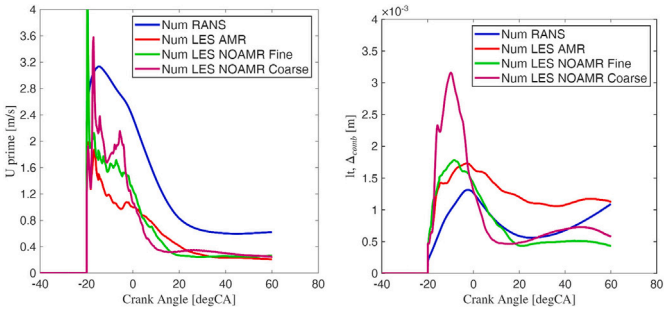


Fig. 26. Numerical results of u' (left) and l_t (right) with three different mesh strategies using the same α value in LES.

the right-hand side, the turbulent length scale estimated from the LES approach correctly reflects the mesh dimensions within the flame, with higher values observed for the coarse mesh case. This confirms that both the AMR and uniform fine-mesh configurations provide acceptable mesh resolution for the combustion simulations.

Having observed that the use of the same α values with a uniform mesh leads to different combustion results for all LES operating conditions, owing to differences in the estimation of u', an ad hoc calibration was performed for the fine-mesh configuration. More specifically, the change in calibration between the AMR and uniform-mesh configurations is attributed entirely to the mesh transitions introduced by AMR, which generate a numerical error in the estimation of the turbulent velocity fluctuations. This interpretation is further supported by Fig. 26, which shows that the two uniform-mesh configurations, namely the coarse and fine meshes without AMR, exhibit nearly identical u' values. This result suggests that the mesh resolution itself, ranging from the coarse to the fine uniform mesh, does not significantly affect the estimated subgrid-scale turbulence intensity. Conversely, the length-scale plot confirms that the LES combustion filter scale differs between the two

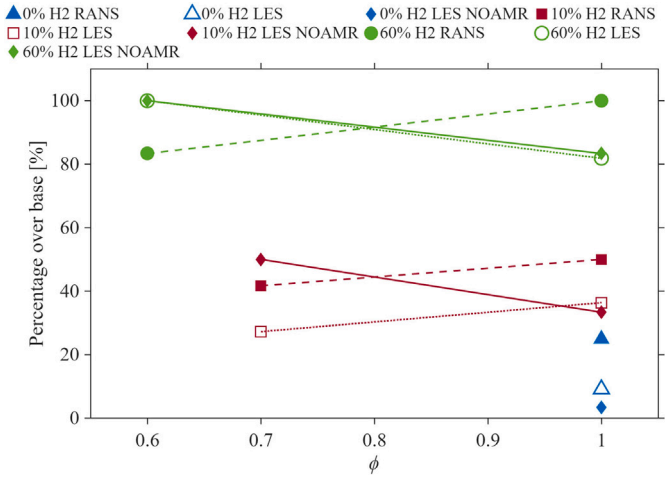


Fig. 27. Comparison of LES and RANS α trends, including cases without AMR, normalized by the case with the highest α value at an intake pressure of 1.2 bar.

configurations as a result of the different mesh resolutions in the flame region. Moreover, recalibrating the uniform-mesh cases removes the numerical artefact affecting the α trends, thereby restoring the original physical interpretation of the calibration parameter, which is intended to compensate only for the intrinsic limitations of the combustion model in predicting flame stretch. Fig. 27 presents the previous results with the addition of the newly calibrated points, obtained using a uniform fine mesh (0.25 mm) throughout the combustion phase. The results obtained with a uniform-mesh configuration (without AMR) demonstrate that, even when the u' modelling issue is removed, the α parameter exhibits the same relative variation, especially when varying the hydrogen content in the mixture. This further supports the conclusion that the limitations of the ECFM in predicting the combustion process are not primarily associated with inaccuracies in the estimation of u'. Instead, they are more closely related to the ability of the model to accurately capture changes in the combustion regime, even when substantially different turbulence-modelling approaches are used to estimate u' and l_t.

5. Conclusion

This work provides a comprehensive analysis of the predictive capability of the well-established flamelet-based ECFM combustion model over a wide range of operating conditions, including variations in hydrogen content in ammonia/hydrogen blends, equivalence ratio, and intake pressure. To evaluate the model behaviour and the associated calibration process, two different turbulence modelling approaches were adopted. In particular, the full dataset was analysed within the RANS framework, while a set of representative operating conditions was further investigated through a dedicated LES numerical campaign, maintaining the same combustion model and engine configuration. All simulated conditions were validated against an extensive experimental dataset obtained from a single-cylinder light-duty engine operated with an ammonia-hydrogen blend. The main conclusions of this work are summarized in the following points:

1. Starting from the RANS numerical results, the analysis of the α parameter variation clearly indicates that a point-to-point calibration is required to cover such a wide range of operating conditions. A more robust calibration behaviour is observed when varying the intake pressure. The calibration trends of the combustion model can be related to the variation of the combustion regime, as reducing the hydrogen content shifts the flame towards higher Karlovitz number conditions, typically within the thin reaction zone regime. Conversely, the required calibration variation decreases when moving from stoichiometric to lean conditions, despite the presence of some outlier cases close to the combustion stability limits.
2. Building on the RANS investigation, a set of representative operating conditions was further examined using the LES approach. The comparison of the relative variation of the α parameter shows that the trends observed in RANS are consistently confirmed by the LES results, highlighting the need for significant recalibration when varying the hydrogen content in the fuel mixture. To further support this analysis, a statistical evaluation based on selected engine error metrics was performed to assess the capability of the combustion model to reproduce experimental data through the calibration of the flame stretch.
3. Following the evaluation of the combustion model performance, a more detailed analysis of the model source terms governing the flame stretch was carried out by comparing RANS results with LES cycles. In particular, the α values obtained from RANS are generally lower than those in LES due to two main reasons. First, the input parameters of the LPF model are not defined in the same way in RANS and LES approaches. While in the RANS formulation the turbulent length scale l_t is well defined through the $k-\varepsilon$ equations, in LES no turbulence length scale is explicitly modelled; instead, the combustion filter scale Δ_{comb} is provided for the evaluation of turbulent strain. More specifically, Δ_{comb} in the LES approach is determined by the mesh resolution and is, in the present numerical results, consistently higher than the RANS turbulent length scale l_t obtained from the RNG $k-\varepsilon$ model, although both quantities remain of the same order of magnitude.
4. Finally, a mesh-related issue associated with the LES–AMR coupling was analysed. It is known from the literature that algebraic estimators of the velocity fluctuation, such as the rotational formulation employed in this work, coupled with a dynamic adaptive mesh refinement (AMR) strategy, can lead to an underestimation of u'. This occurs because the resolved turbulent structures do not have sufficient time to adapt to the finer AMR grid after the mesh refinement process. No significant differences were observed in a dedicated numerical campaign for the relative α variation when adopting a fine uniform mesh (fixed mesh of 0.25 mm) throughout the combustion process.

The numerical results suggest that the limitations in the predictive capability of the ECFM may not be primarily associated with the adopted turbulence description, but rather with the ability of the combustion model to accurately represent different combustion regimes. This conclusion is supported by the consistent calibration trends obtained using two substantially different turbulence modelling approaches, RANS and LES. Despite their different representations of the turbulent flow field and their different approaches to estimating u' and l_t, both approaches exhibit similar variations in the calibrated α parameter across the investigated combustion conditions. This consistency indicates that the underlying modelling error could be primarily associated with the prediction of flame stretch as the combustion regime changes, rather than with the turbulence description itself. These results further highlight the need for a revised formulation of the ECFM model specifically tailored to high Karlovitz number regimes, in order to accurately capture variations in turbulence-flame interaction across a wide range of combustion conditions. The subgrid-scale contribution, in both the RANS and LES approaches, emerges as the primary factor influencing the prediction of flame stretch. Rather than introducing a fitted correlation calibrated over a limited dataset and a restricted range of fuel compositions, improving the formulation of the flame surface density source terms represents a more physically consistent approach to extending the predictive capability of the model. Such an approach is expected to provide greater robustness when both the turbulence characteristics and mixture properties are varied. Moreover, an additional sub-model for estimating the stretch factor I_0 associated with thermo-diffusive effects is required for unstable lean mixtures, in which preferential diffusion

can significantly modify the local flame propagation speed. Accounting for this contribution is therefore necessary to consistently predict the resulting turbulent flame speed across both stable and thermo-diffusively unstable combustion regimes.

CRediT authorship contribution statement

Riccardo Sola: Writing – original draft, Software, Methodology, Formal analysis, Conceptualization. **Daniela Misul:** Writing – review & editing, Methodology. **Mirko Baratta:** Writing – review & editing, Methodology. **Christine Mounaïm-Rousselle:** Writing – review & editing, Data curation. **Pierre Brequigny:** Writing – review & editing, Data curation. **Olivier Colin:** Writing – review & editing, Methodology, Conceptualization.

Declaration of competing interest

The authors declare that they have no known competing financial interests or personal relationships that could have appeared to influence the work reported in this paper.

Acknowledgements

We acknowledge the CINECA award under the ISCRA initiative, for the availability of high-performance computing resources and support. Computational resources were provided by hpc@polito, which is a project of Academic Computing within the Department of Control and Computer Engineering at the Politecnico di Torino (http://www.hpc.polito.it). This publication is part of the project PNRR-NGEU which has received funding from MUR - DM 117/2023.

Data availability

The authors do not have permission to share data.

References

[1] Tornatore C, Marchitto L, Sabia P, Joannon MD. Ammonia as green fuel in internal combustion engines: state-of-the-art and future perspectives. Front Mech Eng Jul 2022. https://doi.org/10.3389/fmech.2022.944201
[2] Chai WS, Bao Y, Jin P, Tang G, Zhou L. A review on ammonia, ammonia-hydrogen and ammonia-methane fuels. Renew Sustain Energy Rev Sep 2021. https://doi.org/10.1016/j.rser.2021.111254
[3] Frigo S, Gentili R. Analysis of the behaviour of a 4-stroke Si engine fuelled with ammonia and hydrogen. Int J Hydrog Energy 2013;38:1607–15. https://doi.org/10.1016/j.ijhydene.2012.10.114
[4] Koike M, Suzuoki T, Takeuchi T, Homma T, Hariu S, Takeuchi Y. Cold-start performance of an ammonia-fueled spark ignition engine with an on-board fuel reformer. Int J Hydrog Energy 2021;46(50):25689–98. https://doi.org/10.1016/j.ijhydene.2021.05.052. https://www.sciencedirect.com/science/article/pii/S0360319921017729.
[5] Zhu T, Yan X, Gao Z, Qiu Y, Zhu L, Huang Z. Combustion and emission characteristics of ammonia-hydrogen fueled SI engine with high compression ratio. Int J Hydrog Energy 2024;62:579–90. https://doi.org/10.1016/j.ijhydene.2024.03.035
[6] Lhuillier C, Brequigny P, Contino F, Mounaïm-Rousselle C. Experimental study on ammonia/hydrogen/air combustion in spark ignition engine conditions. Fuel Jun 2020;269. https://doi.org/10.1016/j.fuel.2020.117448
[7] Lhuillier C, Brequigny P, Contino F, Rousselle C. Performance and emissions of an ammonia-fueled SI engine with hydrogen enrichment. In: SAE technical papers, vol. 2019-September. SAE International; 2019. https://doi.org/10.4271/2019-24-0137
[8] Mercier A, Mounaïm-Rousselle C, Brequigny P, Bouriot J, Dumand C. Improvement of SI engine combustion with ammonia as fuel: effect of ammonia dissociation prior to combustion. Fuel Commun 2022;11:100058. https://doi.org/10.1016/j.jfueco.2022.100058
[9] Zitouni S, Glaznev R, Pitsch H, Beeckmann J, Bréquigny P, Mounaïm-Rousselle C, Halter F. Accounting for buoyancy and ignition influence in the experimental measurement of laminar flame speeds and Markstein lengths from spherical ammonia/air flames. Proc Combust Inst Jan 2025;41. https://doi.org/10.1016/j.proci.2025.105891
[10] Zitouni S, Brequigny P, Mounaïm-Rousselle C. Influence of hydrogen and methane addition in laminar ammonia premixed flame on burning velocity, Lewis number and Markstein length. Combust Flame Jul 2023;253. https://doi.org/10.1016/j.combustflame.2023.112786
[11] Lhuillier C, Brequigny P, Contino F, Mounaïm-Rousselle C. Experimental investigation on ammonia combustion behavior in a spark-ignition engine by means of laminar and turbulent expanding flames. Proc Combust Inst 2021;38:6671–8. https://doi.org/10.1016/j.proci.2020.08.058
[12] Lapointe S, Blanquart G. Fuel and chemistry effects in high Karlovitz premixed turbulent flames. Combust Flame 2016;167:294–307. https://doi.org/10.1016/j.combustflame.2016.01.035
[13] Gaucherand J, Laera D, Schulze-Netzer C, Poinsot T. Intrinsic instabilities of hydrogen and hydrogen/ammonia premixed flames: influence of equivalence ratio, fuel composition and pressure. Combust Flame Oct 2023;256. https://doi.org/10.1016/j.combustflame.2023.112986
[14] Lehmann T, Berger L, Howarth TL, Gauding M, Girhe S, Dally BB, Pitsch H. Comprehensive linear stability analysis for intrinsic instabilities in premixed ammonia/hydrogen/air flames. Combust Flame Mar 2025;273. https://doi.org/10.1016/j.combustflame.2024.113927
[15] Coulon V, Gaucherand J, Xing V, Laera D, Lapeyre C, Poinsot T. Direct numerical simulations of methane, ammonia-hydrogen and hydrogen turbulent premixed flames. Combust Flame Oct 2023;256. https://doi.org/10.1016/j.combustflame.2023.112933
[16] Gaucherand J, Laera D, Schulze-Netzer C, Poinsot T. DNS of turbulent premixed Ammonia/Hydrogen flames: the impact of thermo-diffusive effects. Flow Turbul Combust 2024;112:587–614. https://doi.org/10.1007/s10494-023-00515-1
[17] Sola R, Baratta M, Misul D, Santonocito F, Kawanabe H. Premixed hydrogen-methane combustion modelling with ECFM in a pre-chamber equipped RCEM. Fuel 2026;415:138455. https://doi.org/10.1016/j.fuel.2026.138455. https://www.sciencedirect.com/science/article/pii/S0016236126002085.
[18] Sola R, Baratta M, Misul D, Rousselle C, Brequigny P, Colin O. Evaluation of flamelet-based combustion models for hydrogen-ammonia spark-ignition engines. In: CO_2 reduction for transportation systems conference; 2026. https://doi.org/10.4271/2026-37-0027
[19] Benajes J, Novella R, Gomez-Soriano J, Barbery I, Libert C, Rampanarivo F, Dabiri M. Computational assessment towards understanding the energy conversion and combustion process of lean mixtures in passive pre-chamber ignited engines. Appl Therm Eng 2020;178:115501. https://doi.org/10.1016/j.applthermaleng.2020.115501. https://www.sciencedirect.com/science/article/pii/S1359431120329835.
[20] Misdariis A, Robert A, Vermorel O, Richard S, Poinsot T. Numerical methods and turbulence modeling for LES of piston engines: impact on flow motion and combustion. Oil Gas Sci Technol - Revue de l IFP 2013;69:83–105. https://doi.org/10.2516/ogst/2013121
[21] Han Z, Reitz RD. Turbulence modeling of internal combustion engines using RNG k-ε models. Combust Sci Technol 1995;106:267–95. https://doi.org/10.1080/00102209508907782
[22] Smagorinsky J. General circulation experiments with the primitive equations: i. The basic experiment. Mon Weather Rev 1963;91(3):99–164. https://doi.org/10.1175/1520-0493(1963)091<0099:GCEWTP>2.3.CO;2. https://journals.ametsoc.org/view/journals/mwre/91/3/1520-0493_1963_091_0099_gcewtp_2_3_co_2.xml.
[23] Berni F, Cicalese G, Fontanesi S. A modified thermal wall function for the estimation of gas-to-wall heat fluxes in CFD in-cylinder simulations of high performance spark-ignition engines. Appl Therm Eng 2017;115:1045–62. https://doi.org/10.1016/j.applthermaleng.2017.01.055
[24] Senecal PK, Pomraning E, Wang M. Development of a species-based extended coherent flamelet model (SB-ECFM) for gasoline direct injection engine (GDI) simulations. Tech. Rep 2018. https://proceedings.asmedigitalcollection.asme.org.
[25] Colin O, Truffin K. A spark ignition model for large eddy simulation based on an FSD transport equation (ISSIM-LES). Proc Combust Inst 2011;33:3097–104. https://doi.org/10.1016/j.proci.2010.07.023
[26] Stagni A, Arunthanayothin S, Dehue M, Herbinet O, Battin-Leclerc F, Bréquigny P, Mounaïm-Rousselle C, Faravelli T. Low- and intermediate-temperature ammonia/hydrogen oxidation in a flow reactor: experiments and a wide-range kinetic modeling. Chem Eng J Sep 2023;471. https://doi.org/10.1016/j.cej.2023.144577
[27] Pope SB. Turbulent flows. Cambridge University Press; 2001.
[28] Piscaglia F, Montorfano A, Onorati A. Towards the LES simulation of IC engines with parallel topologically changing meshes. SAE Int J Engines 2013;6:926–40. https://doi.org/10.4271/2013-01-1096
[29] Richard S, Colin O, Vermorel O, Benkenida A, Angelberger C, Veynante D. Towards large eddy simulation of combustion in spark ignition engines. Proc Combust Inst 2007;31 II:3059–66. https://doi.org/10.1016/j.proci.2006.07.086
[30] Szanthoffer AG, Papp M, Nagy T, Turányi T. Assessing the performance of recent detailed NH_3 and NH_3/H2 combustion mechanisms. Combust Flame 2026;287:114878. https://doi.org/10.1016/j.combustflame.2026.114878. https://linkinghub.elsevier.com/retrieve/pii/S0010218026001148.
[31] Moses JK, Tivfa TA, Qasem NA, Alquaity AB. Combustion characteristics of hydrogen, ammonia, and their blends: a review. Fuel May 2025. https://doi.org/10.1016/j.fuel.2025.134404
[32] Suillaud E, Truffin K, Colin O, Veynante D. Direct numerical simulations of high Karlovitz number premixed flames for the analysis and modeling of the displacement speed. Combust Flame Feb 2022;236. https://doi.org/10.1016/j.combustflame.2021.111770
[33] Poinsot T, Veynante D. Theoretical and numerical combustion. Prog Energy Combust Sci Jan 2005;28.
[34] Peters N. The turbulent burning velocity for large-scale and small-scale turbulence. J Fluid Mech 1999;384:107–32. https://doi.org/10.1017/S0022112098004212
[35] Colin O, Ducros F, Veynante D, Poinsot T. A thickened flame model for large eddy simulations of turbulent premixed combustion. Phys Fluids 2000;12:1843–63. https://doi.org/10.1063/1.870436
[36] Mehl C, Liu S, Colin O. A strategy to couple thickened flame model and adaptive mesh refinement for the LES of turbulent premixed combustion. Flow Turbul Combust 2021;107:1003–34. https://doi.org/10.1007/s10494-021-00261-2